Characteristics of Dust Storms Generated by Trapped Waves in the Lee of Mountains

Amato T. Evan,[a] William C. Porter,[b] Rachel Clemesha,[a] Alex Kuwano,[a] and Robert Frouin,[a]

[a] *Scripps Institution of Oceanography, University of California San Diego*

[b] *Department of Environmental Sciences, University of California Riverside*

Corresponding author: Amato Evan, aevan@ucsd.edu

ABSTRACT: In-situ observations and output from a numerical model are utilized to examine three dust outbreaks that occurred in the northwestern Sonoran Desert. Via analysis of these events it is shown that trapped waves generated in the lee of an upwind mountain range produced high surface wind speeds along the desert floor and the observed dust storms. Based on analysis of observational and model output general characteristics of dust outbreaks generated by trapped waves are suggested, including dust layer depths and concentrations that are dependent upon wave phase and height above the surface, emission and transport associated with the presence of a low-level jet, and wave-generated high wind speeds and thus emission that occurs far downwind of the wave source. Trapped lee waves are ubiquitous in the Earth's atmosphere and thus it is likely that the meteorological aspects of the dust storms examined here are also relevant to understanding dust in other regions. These dust outbreaks occurred near the Salton Sea, an endorheic inland body of water that is rapidly drying due to changes in water use management. As such, these findings are also relevant in terms of understanding how future changes in size of the Salton Sea will impact dust storms and air quality there.

SIGNIFICANCE STATEMENT: Dust storms are ubiquitous in the Earth's atmosphere, yet the physical processes underlying dust emission and subsequent transport are not always understood, in-part due to the wide variety of meteorological processes that can generate high winds and dust. Here we use in-situ measurements and numerical modeling to demonstrate that vertically trapped atmospheric waves generated by air flowing over a mountain are one such mechanism that can produce dust storms. We suggest several features of these dust outbreaks that are specific to their production by trapped waves. As the study area is a region undergoing rapid environmental change, these results are relevant in terms of predicting future dust there.

1. Introduction

Aeolian dust is one of the most pervasive aerosols in the Earth's atmosphere (Huneeus et al. 2011). Dust alters the planet's radiative budget and hydrological cycles via aerosol direct and indirect effects (Choobari et al. 2014) and affects nutrient cycling in the marine and terrestrial ecosystems where dust emission and deposition occurs (Field et al. 2010). As such, there is a need to understand how planetary climate change has–and will continue to–influence the processes of dust emission, transport, and deposition, the so-called dust cycle (Shao et al. 2011), as well as to understand how those forced changes in the dust-cycle feedback onto the Earth's climate (Kok et al. 2018). However, studies examining the representation of dust in model output from the fifth and sixth Climate Model Intercomparison Projects have identified model biases in the dust mean state, poor reproduction of historical dust variability, and insufficient sensitivity of dust emission to changes in surface conditions (Pu and Ginoux 2018; Zhao et al. 2022), casting doubt on our ability to model future dust.

Improving understanding of the physical processes leading to dust emission and transport can lead to advances in the representation of dust in models. Although there is a growing body of knowledge of the meteorological processes underlying dust storms (Knippertz 2014), there remains a dearth of representative in-situ observations in dust emitting regions, which is not entirely surprising given that most dust outbreaks occur in sparsely populated regions (Prospero et al. 2002) where challenges associated with access can be significant (e.g., Giles 2005). This study aims to add to understanding of the meteorological processes affecting dust storms by examining measurements made during three dust outbreaks in a region of southeastern California, with a specific focus on the role of complex terrain in shaping the characteristics of the high winds and lofted dust. Previous studies have identified several processes associated with orographically-forced flow that result in high winds and dust lofting, including gap flow (Evan et al. 2016; Jiang et al. 2009; Todd et al. 2008), downslope winds due to orographic precipitaction and latent cooling of air (Knippertz et al. 2007; Evan et al. 2022c), generic Foehn events (Gläser et al. 2012; Evan 2019), and lee-side rotor circulations (Grubišić and Billings 2007; Pokharel et al. 2017). Here we focus on the role of trapped lee-waves in generating dust outbreaks.

Trapped lee waves are a class of orographically forced waves (i.e., generated by air flowing over a mountain range) for which the waves are trapped in the lower atmosphere, rather than propagating upwards through the troposphere (Nappo 2013), propagating laterally well beyond the location of wave generation (Durran 2003). Vertical variations in stability and shear in the upstream flow (i.e., upwind of the mountain range) give rise to trapped waves (Scorer 1949), and temporal changes in these properties result in non-stationary waves (Ralph et al. 1997). Trapped waves can give rise to rotors in the downslope flow, in which rapid vertical ascent in the upward branch of a wave can produce flow separation at the surface and reversed surface winds under the wave crest (Doyle and Durran 2002), and modify (both accelerate and decelerate) surface wind speeds far beyond the wave source (Durran 1986).

While there is a rich history of scholarly work on the topic of trapped lee waves (c.f., Smith 2019), to the best of our knowledge studies connecting trapped waves to dust emission and transport have been limited to the Owen's Valley, and more strongly focused on the dynamics of the lee-side circulation than the characteristics of the subsequent dust storms (Grubišić et al. 2008; De Wekker and Mayor 2009; Jiang et al. 2011; Strauss et al. 2016). Additionally, Owen's Valley is narrow and consequently waves forming in the lee of the Eastern Sierra are distinct from trapped lee waves that are able to propagate long distances downwind of the region of wave generation. Given the ubiquity of trapped lee waves in the Earth's atmosphere it is at least plausible that these orographically forced phenomena are responsible for a non-negligible fraction of the global dust uplift (e.g., downwind of the Atlas or Andes mountains).

Our area of interest is the Salton Basin, a sub-sea level terminal basin located at the northwestern corner of the Sonoran Desert that is part of the greater Salton Trough, a northwest-southeast oriented rift valley along the San Andreas Fault (Fig. 1). At the lowest elevations of the basin lies the Salton Sea, an endorheic body of water having an average surface height of -72.7 m AMSL in 2021 (`dashboard.waterdata.usgs.gov` *accessed on March 24, 2022*). Dust storms are a frequent occurrence in this region (Evan 2019), which is due in part to the prevalence of erodible soils (Buck et al. 2011; Sweeney et al. 2011). The Salton Sea was accidentally created in 1905 during an attempt to irrigate the southern portion of the Salton Trough (the Imperial Valley), but more recently the volume of the Sea has been declining due to a 2003 water transfer agreement that resulted in diversion of water from the Sea. Consequently, the size of the Salton Sea is rapidly declining (Poudel et al. 2021).

Playa sources represent a significant fraction of all dust emission associated with human activity (Ginoux et al. 2012), and the drying of bodies of water in arid regions increases the incidence and intensity of dust storms there (Zucca et al. 2021). A simulation of a single dust event in the Salton Basin estimated an approximately 10% increase in dust burden with a nearly 40% growth in the playa surface (Parajuli and Zender 2018), which is significant given that the playa is surrounded by desert dust sources that are vastly larger in spatial extent. Other work has shown adverse health effects from exposure to dust emitted from the playa (Burr et al. 2021; Biddle et al. 2021), which contains anthropogenic trace metals (Frie et al. 2019). As such, improving understanding of the meteorology underlying dust events in this region is useful in terms of understanding the changing dust burden and the associated human health impacts.

The remainder of this article is organized as follows. In Section 2 we describe the observational data and model output used in the study. In Section 3 we examine the meteorological and physical aspects of three dust storms via measurements and model output. In Section 4 we discuss general characteristics of dust storms generated by trapped lee waves. In Section 5 we summarize the work presented here, note the broader implications of the findings, and suggest additional observations and modeling studies to address remaining questions.

2. Observations and Model

We start by describing the region of interest (Fig. 1). The Salton Basin is an arid endoheric basin that typically receives less than 100 mm of precipitation each year (Stephen and Gorsline 1975; NCEI). The morphology of the area includes alluvial fans, sand and sand dunes, dry washes, paleo lakebed, and rock and vegetated surfaces (IID 2016). Within the basin, the Salton Sea is a spatially large yet shallow inland body of water. Agriculture land is found immediately to the north and south of the Salton Sea, whereas the Anza desert, from which many dust storms in the area originate, lies immediately to its west (Fig. 1a). The Basin is bounded to the west by the Peninsular Range, to the north by the San Bernardino Mountains, and to the east by the Transverse Range, while the topography gradually slopes upward to the south before dropping into the Colorado River Delta (Fig. 1b).

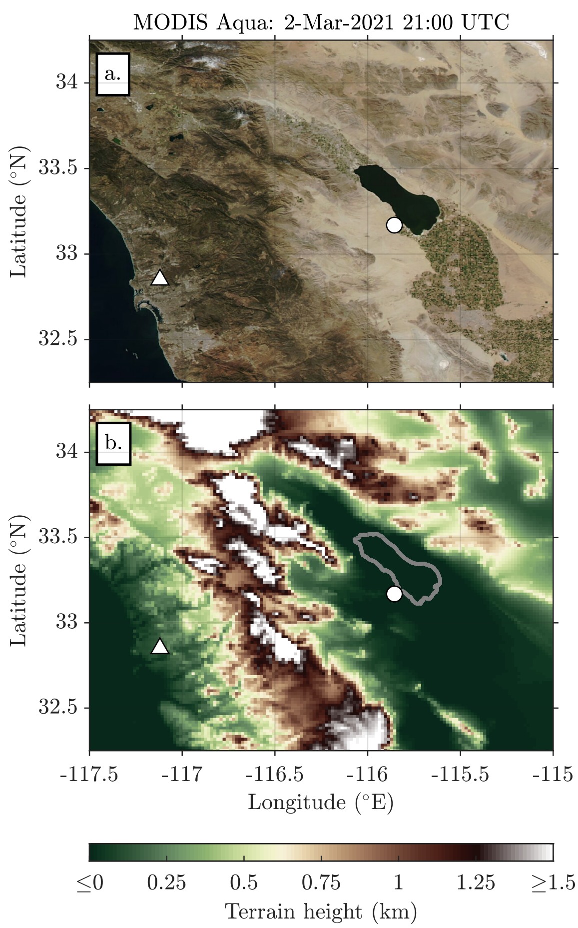

FIG. 1. Terrain of the region of interest. Shown in 1a is a true color image acquired from MODIS-Aqua on March 2, 2021 at 21:00 UTC. Shown in 1b is an elevation map of the same region. The approximate shoreline of the Salton Sea during March 2021 is indicated by the gray contour. The locations of the field and the NKX radiosonde sites are indicated by the white circles and triangles, respectively, in both panels. The desert that lies immediately west of the field site is the source region for the airborne dust measured at the site.

a. Field site and in-situ Observations

Much of the observational data presented here was collected from a field site located near the current western coastline of the Salton Sea, at approximately 33.2 N and -115.9 E (Fig. 1). The site is adjacent to a large citrus and date palm farm, which provides physical security for the station and allows for access to a stable source of power for instrumentation and telemetry. The landscape immediately surrounding the site is characterized by narrow dry washes and cobbles distributed over silt-dominated paleo lakebed with sparse shrub vegetation.

An AERONET CIMEL Electronique Sun–sky photometer is located at the site, which is used to measure Sun collimated direct beam irradiance and directional sky radiance at 8 spectral bands centered on 1020, 870, 675, 440, 936, 500, 380, and 340 nm (Holben et al. 1998). The instrument base is mounted approximately 2 m above ground level. Direct solar irradiance measurements are made at 5-minute intervals. Here we utilize data from the AERONET Level 1.5 products processed by the Version 3 AERONET algorithm, which provides fully automatic cloud screening and instrument anomaly quality controls in near-real-time (Giles et al. 2019). We include dusty observations that were erroneously classified as cloud-contaminated using the restoring algorithm described in Evan et al. (2022a).

Located at the field site is a Vaisala CL51 ceilometer, which is a single lens lidar system that makes continuous profiles of attenuated backscatter at a nominal wavelength of 910 nm and up to heights of 15 km. The CL51 range corrected backscatter profiles used here are generated at a 36 s temporal resolution and a 10 m vertical resolution. In addition to cloud detection, ceilometers, including the CL51, have shown to be useful in the detection of aerosol layers in the lower troposphere (Münkel et al. 2007; Wiegner et al. 2014; Jin et al. 2015; Marcos et al. 2018; Yang et al. 2020). The Vaisala processing software for the CL51 measurements, BLView, produces retrievals of vertical profiles of extinction σ and optical depth τ from the backscatter profiles for the clear-sky atmosphere below 5 km. Although details regarding the retrieval process used in BLView are not publicly available, we are able to approximately reproduce the extinction profile retrievals using the methods described in (Fernald 1984), as discussed in Evan et al. (2022c). We calibrate the 910 nm aerosol optical depth (AOD) retrieved from the CL51, which is obtained by integrating the retrieved extinction profiles in the vertical dimension to an equivalent 500 nm value by comparing values of 500 nm

AOD from AERONET to the 910 nm AOD retrieved from the CL51, following the methods in Evan et al. (2022a).

At this site also sits a cabled Vantage Pro2 Davis Met Station, which has a suite of sensors including temperature and humidity sensors under a passive radiation shield, a wind anemometer, a barometer, and rainfall measurements. Data are logged at a 1-min interval. The site anemometer sits approximately 2-m above ground level. The 2-m wind speed and gust measurements were calibrated to an equivalent 10-m wind speed value by multiplying the 2-m values by a factor of 1.37, which was empirically derived via comparison to an adjacent 10-m mounted anemometer (Evan et al. 2022a). We note that at present only hourly averaged values are available from the 10-m anemometer, which is managed by the local water and power utility, Imperial Irrigation District.

Vertical profiles of temperature, humidity, pressure and wind are obtained from Vaisala RS-41 sondes launched at the site on March 9, 2021 (at 1203, 1505, 1803, 1934, 2102, 2234, and 2359 UTC), March 15, 2021 (at 2114 and 2320 UTC), and February 15, 2022 (at 2105, 2242, and 2340 UTC). Lastly, all heights from soundings and the CL51 are referenced to ground level of the station, which sits approximately 32 m below mean sea level. Radiosonde, meteorological station, and ceilometer profiles made at the field site are permanently archived and publicly available (Evan et al. 2022b).

b. Other Data

In addition to the measurements made at the field site we utilize surface meteorological and PM_{10} measurements made from stations around the Salton Sea. We examine measurements of PM_{10} since in this area elevated values of PM_{10} are an unambiguous indication of the presence of suspended dust, whereas, for example, $PM_{2.5}$ may indicate the presence of dust as well as other local sources of particulates. The meteorological and PM_{10} data were accessed via the MesoWest network (Horel et al. 2002) and the California Air Resources Board Air Quality and Meteorological Information System. We also utilize imagery from a 360° Roundshot web camera that is located 28 km west of the field site at an elevation of 300 m AGL, which are available at approximately 10 min intervals during daytime hours. We incorporate into our analysis satellite imagery from the Moderate Resolution Imaging Spectrometer (MODIS) flying onboard the Aqua satellite, which were generated from the NASA Earth Observing System Data and Information System (EOSDIS)

Worldview application. We also generated imagery from radiance measurements made by the Advanced Baseline Imager (ABI) flying onboard GOES-17. These data were accessed from the NOAA Comprehensive Large Array-data Stewardship System. We examine measurements collected from radiosondes launched from the NKX sounding station, which is near the coastline (white triangle, Fig. 1), where radiosondes are launched twice daily at 00:00 and 24:00 UTC. Three-hourly output from the North American Regional Reanalysis (NARR), which is provided on 29 vertical layers at a 32-km horizontal resolution, is used to examine the synoptic environment associated with the dust outbreaks studied here (Mesinger et al. 2006).

c. WRF Model

Numerical simulations of the meteorology underlying the dust cases examined here were made using the Advanced Research version of the Weather Research and Forecasting (WRF) Model (Skamarock et al. 2019) version 4.3. The model was run using 3-domain, nested 2-way interactive grid with horizontal resolutions of 15, 5, and 1 km (Fig. 2). The model was initialized using data from the Global Forecast System (GFS) output (NCEP 2013) at 06:00 UTC on March 8 2021, March 14 2022, and February 14 2022, and was integrated forward for the subsequent 72 hours for each case with the lateral boundaries of the outtermost domain continuously forced by the GFS output. WRF model output shown here is from the innermost domain.

The model top is at 10 hPa and 51 sigma vertical levels are employed, with the highest vertical resolution found in the lower troposphere. Approximately 7 half-sigma levels are found in the lowest kilometer AGL, with the first level at a height of 27 m AGL. The output shown here is from simulations using the Mellor–Yamada–Janjić (Janjić 1994) planetary boundary layer scheme, which, when compared to other boundary layer schemes, was found to best reproduce in-situ observations, particularly the surface wind speeds, in the region (Evan et al. 2022c). The model physics parameterizations used in this study are shown in Table 1. Comparisons of WRF output to surface wind measurements at the field site and radiosondes launched during the dust outbreaks considered here can be found in Supplemental Figures S1–S13.

We also conduct simulations using the WRF-Chem model (Grell et al. 2005; Fast et al. 2006; Peckham et al. 1991), employing the GOCART aerosol scheme without ozone chemistry (Chin et al. 2000; Ginoux et al. 2001) and the Air Force Weather Agency dust emission scheme (AFWA

Table 1. Physics schemes employed in the WRF simulations

Parameterization	Scheme
Planetary boundary layer	Mellor–Yamada–Janjić (Janjić 1994; Janić 2001)
Surface layer	Monin-Obukhov with Janjic Eta (Monin and Obukhov 1954; Janić 2001)
Land surface physics	Noah Land Surface Model (Chen and Dudhia 2001)
Longwave & shortwave radiation	RRTMG & RRTMG (Iacono et al. 2008)
Purdue Lin scheme	(Chen and Sun 2002)
Cumulus scheme (5 & 15 km domains)	Grell3D (Grell 1993; Grell and Dévényi 2002)

LeGrand et al. 2019), with other model parameterizations, setup, and forcing identical to that described for the WRF simulations (Table 1). The AFWA emissions scheme, which uses a modified version of the saltation-based dust emission function of Marticorena and Bergametti (1995), is one of several available by default in current versions of WRF-Chem. This scheme represents an update to the earlier GOCART-WRF emissions scheme, incorporating separately modeled saltation processes driving subsequent dust emissions rather than the single-step parameterization used previously. Since its addition to WRF-Chem, the AFWA scheme has been used and evaluated

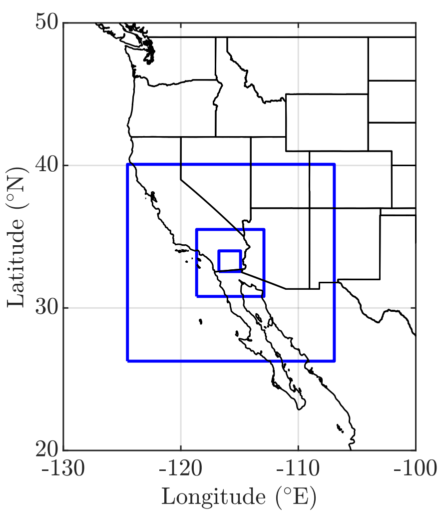

Fig. 2. Domains for the nested WRF simulations. Plotted in blue are the horizontal extents of the nested domains utilized in the WRF simulations. The horizontal resolutions of the outtermost to innermost domains are 15, 5, and 1 km, respectively.

in dust modeling research and case studies around the world (e.g. Yuan et al. 2019; Kim et al. 2021; Miller et al. 2021). In the model dust in the size range of 0.2-20 μm is simulated in 5 bins.

When comparing the model simulated dust to aerosol measurements at the field site and surface PM_{10} measurements at a number of locations around the Salton Sea we found that the model produced too much dust at weak wind speeds and too small an increase in dust as the wind speed increased. We also found via comparison to surface PM_{10} measurements that dust surface concentrations were biased low in the region of the research site, and biased high to the north and south of the site (not shown). These biases persisted across two different soil erodibility input maps, including the default GOCART topographic erodibility dataset of Ginoux et al. (2001), as well as the more recent data set of Parajuli and Zender (2017). Based on their consistency across erodibility map inputs, we suspect that these biases are related to other surface property inputs, such as soil and land surface cover type.

Due to concerns over the representation of dust emission in the model we only utilize output from a WRF-Chem simulation of the dust outbreak on March 15, 2021 in order to examine the general relationship between trapped lee wave phase and the vertical and horizontal distribution of dust (Section 4). We leave improvement of the representation of modeled dust in this region for future work.

d. Salton Sea Extent

The extent of the Salton Sea was estimated using MODIS Aqua visible satellite imagery from March 2, 2021 (Fig. 1a). To estimate the shoreline we applied an arbitrary threshold to the reflectances of each of the three image color channels (i.e., red, green, blue) in order to distinguish the dark Salton Sea against the bright desert surface, manually excluding any pixels that were dark enough to pass this threshold test from the vegetated croplands to the south of the sea. We then used these data to define the shoreline of the sea (gray contour, Fig. 1b). The shoreline estimate is used as a visual aid in several figures found throughout this manuscript.

3. Characteristics of the Dust Storms

Here we consider three dust outbreaks within the Salton Basin: March 9 and 15, 2021, and February 15, 2022. When convenient we only refer to these cases using their respective months and days. These events were chosen because of the similarities in their meteorological aspects and dust characteristics, and the availability of radiosonde measurements made at the field site.

a. Synoptic Situation

We first describe the synoptic environments for the three dust events considered here. For all cases streamlines and heights of the 500 hPa pressure surfaces from NARR show an upper level low

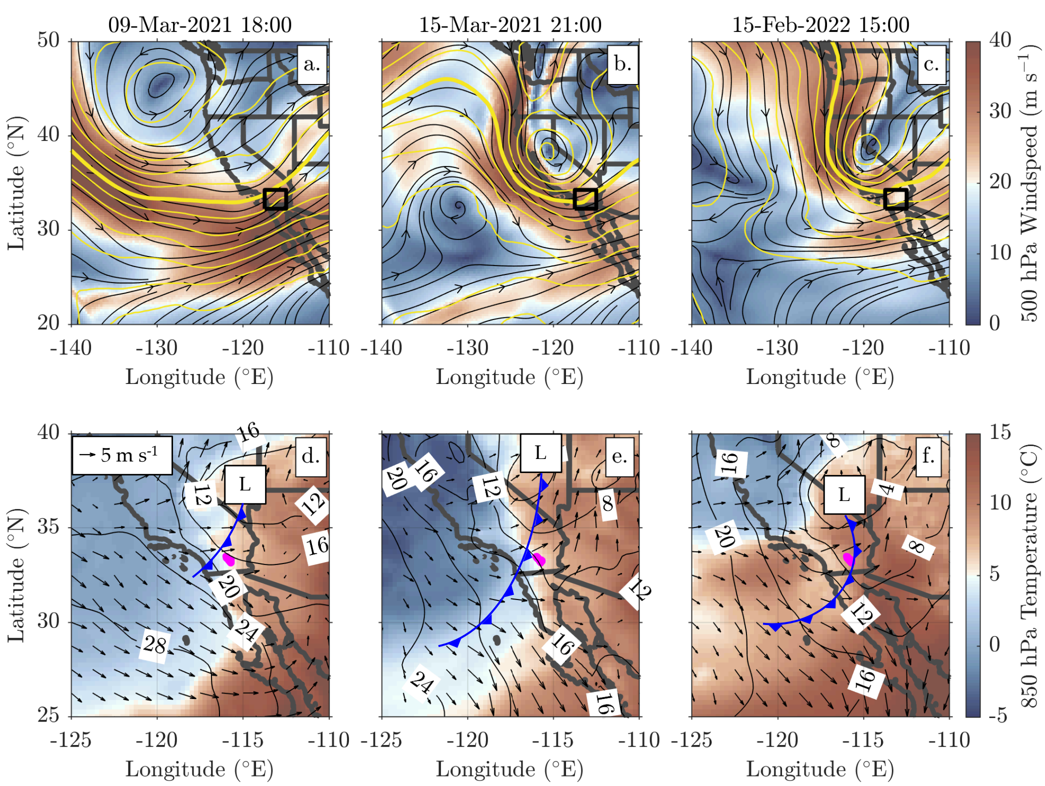

FIG. 3. Synoptic situations immediately preceding the dust outbreaks: March 9, 2021 at 18:00 UTC (3a, d), March 15, 2021 at 21:00 UTC (3b, e), and February 15, 2022 at 15:00 UTC (3c, e). Shown in the top row (3a–c) are maps of NARR 500 hPa wind speeds (shading), streamlines (black), and heights (yellow contours). Heights of the 500 hPa pressure surfaces are represented by the yellow contours at intervals of 5 dm, with the thick contour representing the 560 dm surface. The black box indicates the area shown in Fig. 1. Show in the bottom row (3d–f) are maps of 850 hPa temperature (shading), sea level pressure (black), and vector winds (arrows). Cold fronts (blue) and surface lows (boxed "L") locations are based on NOAA Weather Prediction Center surface analysis. Sea level pressure contours are hPa greater than 1000 hPa. The magenta shading represents the location of the Salton Sea. The horizontal extents of the maps in the top and bottom rows are not identical.

displaced to the northwest of the region of interest, with the lows' centers of action approximately located at 45° and -130°E on March 9, 2021 (Fig. 3a), and 40°N and -120°E on March 15, 2021 and February 15, 2022 (Figs. 3b, c, respectively). For each case the elevated lows direct westerly flow across the region of interest (black squares), with all exhibiting tightly packed height contours and cross barrier (i.e., westerly) wind speeds greater than 20 m s^{-1}. We note that that for the March 9 case the westerly flow is driven by both the broad low located to the north over the Pacific and an anti-cyclone located to the southeast (anti-cyclone not seen in Fig. 3a). Sea level pressure contours for these three cases show surface low pressure centers north of the Salton Sea and near exit regions of the the upper level jets, with trailing cold fronts pushing through the Salton Basin at approximately 18:00, 21:00, and 15:00 UTC (Figs. 3d, e, f, respectively). Temperatures and vector winds at 850 hPa imply low-level northwesterly cold air advection behind the fronts and westerly flow directed at the coastline and over the Salton Sea. The synoptic situations for these cases are similar to that described for dust outbreaks occurring on February 22, 2020 (Evan et al. 2022c) and March 14, 2018 (Evan 2019).

The characteristics of these mature cyclone wave and frontal systems (Fig. 3) generate unique conditions that are favorable for trapping waves, including low-level cold air advection below a westerly jet streak. For the March 9 case (Figs. 3a, d) the upper level trough is open and exhibits a slight negative tilt. Vertical profiles of potential temperature θ and wind speed and direction made from radiosondes launched from the NXK sounding station (see location in Fig. 1) at 12:00 UTC on this day show a 5 C increase in θ in the 725-775 hPa layer (Fig. 4a), which is within a deeper layer (700-800 hPa) of backing winds (Fig. 4c), implying low level cold air advection and cold frontal passage. The sounding made 12 hours later on this day, and after the surface front had passed over the Salton Sea region, shows lifting of the isentropic surfaces from 500-800 hPa (Fig. 4a), indicating a deeper layer of cold air. The 30 m s^{-1} increase in wind speed from 300-500 hPa reflects displacement of the associated jet streak over the region (Fig. 4b). The westerly flow throughout much of the troposphere in the later sounding (Fig. 4c) reflects the strongly zonal nature of the jet at this latitude, which results in part from the continued deepening and southward migration of the low at -130°E and 45°N (not shown).

The low in the March 15 case (Figs. 3b, e) is better developed than that for March 9, exhibiting a neutrally tilted trough digging down the western US coastline. The NXK soundings from this day (Figs. 4d–f) are similar to those from March 9 in several ways, including a 6 C increase in θ at 850 hPa and a layer of backing winds from 800-850 hPa. The sounding made 12 hours later shows lifting of the θ inversion layer to 775 hPa and the layer of backing winds to 775-825 hPa heights. The later sounding also suggests warm air advection in the 750-600 hPa layer, as evidenced by the veering flow from 750-600 hPa and similarity in θ at those heights over the 12-hour time period. Similar to the March 9 case is the presence of a westerly jet with maximum wind speeds at 400-300 hPa.

Lastly the February 15 positively-tilted short wave trough (Fig. 3c) was a fast-moving system and neither NXK sounding for this day exhibits clear signs of cold frontal passage (Figs. 4g–i). The measurements indicate a large 8 C increase in θ at 870 hPa in the 12:00 UTC sounding, that lifts to approximately 775 hPa 12 hours later, with cooling throughout the 400-900 hPa heights during this time period. The latter sounding also shows an approximately 15 m s^{-1} increase in wind speed

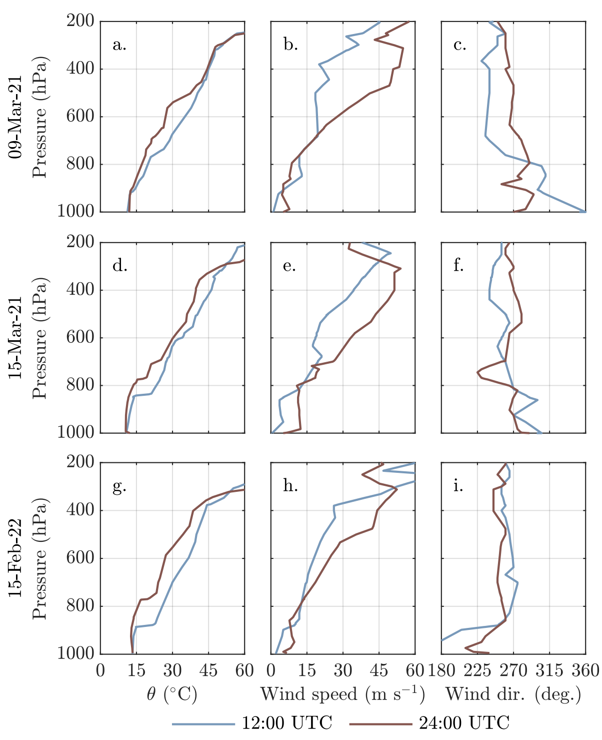

FIG. 4. Measurements from soundings made at the NKX station (see location in Fig. 1). Shown are vertical profiles of potential temperature θ (4a, d, g), wind speed (4b, e, h), and wind direction (4c, f, i) collected from radiosondes launched at 12:00 (light blue) and 24:00 (rust) UTC on March 9, 2021 (4a–c), March 15, 2021 (4d–f), and February 15, 2022 (4g–i).

during this period in the 500-400 hPa layer. Noting that the veering flow below 850 hPa may be the result of surface friction rather than indicating warm air advection, both radiosondes suggest a deep layer of positive zonal flow.

As we discuss in Section 4, these profiles all exhibit characteristics favorable to the generation of trapped lee waves, including low-level cold air advection, with warm air advection aloft in the February 15 case, strongly zonal (i.e., cross-barrier) flow, and positively sheared winds, especially above the heights of the mountain ridges, which in Fig. 4 is approximately located in the 850-800 hPa range.

Within the Salton Basin the passage of these three frontal systems generated a similar response in the surface meteorological conditions. During each the 30-minute averaged surface wind speeds U_s and gusts measured at the field site exceeded 10 and 20 m s^{-1}, respectively, and were westerly in direction (Fig. 5). The persistently westerly flow during the dust outbreaks is in contrast to the typical patterns of wind speed and direction in the basin, which can be characterized as a thermally-driven daytime upslope (easterly) and downslope (westerly) circulation forced by the mountains that lie to the west of the site (e.g., March 6–8, March 12–14 Fig. 5a).

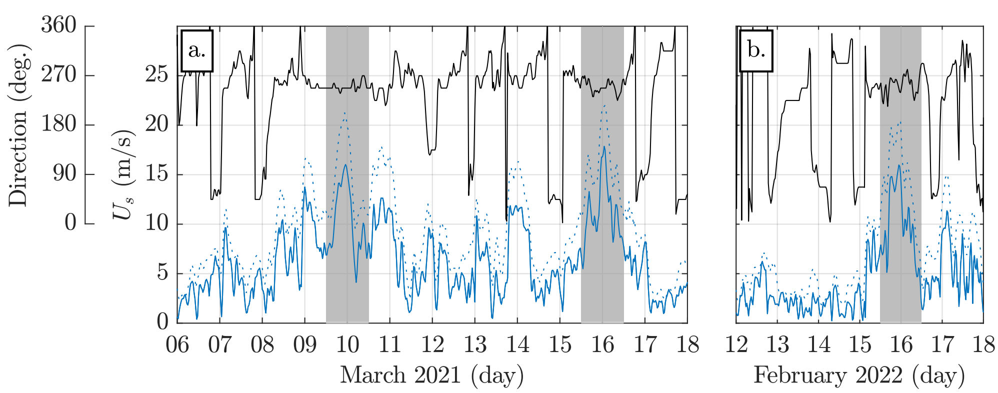

FIG. 5. Time series of surface meteorological measurements made from the field site during March 2021 (5a) and February 2022 (5b). Plotted are 30-minute averaged values of surface wind speed U_s (blue solid line), wind gust speed (blue dotted line), and wind direction (black solid line), with the value of direction indicated by the left-most vertical axis. The gray shaded regions indicate 24-hour periods commencing at 12:00 UTC on March 9 and March 15, 2021, and February 15, 2022, during which the dust outbreaks occurred.

b. Observations of Dust

We next consider the spatial and temporal variability of the dust generated by the high winds present over the Salton Basin. In order to simultaneously visualize wind speed and direction and PM_{10} we generated modified versions of wind roses. For each, the station physical location is at the center point of the rose. Concentric circles indicate wind speed ranges, where the area from the center point to the first concentric circle represents wind speeds in the range of 0-4 m s^{-1}, the area from the first to the second circles represents wind speeds in the range of 4-8 m s^{-1}, and so on in increments of 4 m s^{-1}. The radial divisions represent wind direction. Shading refers to the natural logarithm of the maximum hourly PM_{10} measured for a given wind speed and direction range, where ln PM_{10} values ≥ 5 are above the US EPA 24-hour air quality standard of 150 μg m^3. The data displayed in Fig. 6 corresponds to the time periods highlighted in gray in Fig. 5. Hourly-averaged PM_{10} and wind speed measurements are used to generate these plots.

For all of three cases PM_{10} values exceeding 150 μg m^{-3} (ln $PM_{10} \geq 5$) were observed for at least five of the seven stations, with PM_{10} exceeding 150 μg m^{-3} at all stations during the March 15 case (Fig. 6b). At the northernmost station the strongest wind speed and PM_{10} values occur during northwesterly winds, likely due to flow channeling through Banning Pass (Ryerson et al.

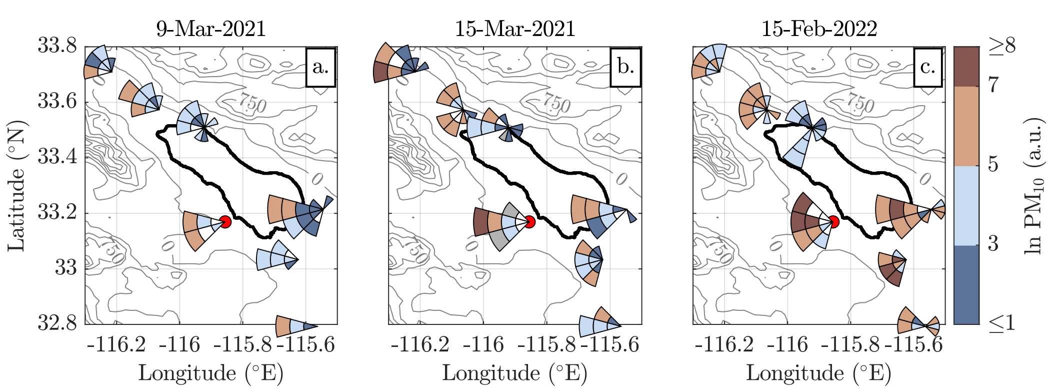

FIG. 6. Modified wind roses indicating peak concentrations of PM_{10} during the three dust outbreaks. Shown in each map are roses (see text for description) made from measurements collected during the dust outbreaks on March 9 (6a) and March 15, 2021 (6b), and February 15, 2022 (6c). Gray shaded rose sections in 6b indicate wind speeds and directions for which corresponding PM_{10} measurements were missing. The gray contours represent surface elevations at intervals of 250 m, and the thick black line represents an estimate of the Salton Sea shoreline in March 2021. The location of the field site is indicated by the red circular marker.

2013), which sits at the northern terminus of the Salton Trough (Fig. 1b). Further to the south the strongest wind speeds and PM_{10} values correspond to increasingly westerly flow, which reflects the widening of the basin and the proximity of the Anza desert, which lies to the west of the Salton Sea and is upwind of the field site (Fig. 1a). Based on the prevalence of measurements for which ln $PM_{10} \geq 5$, the February 15 event exhibited the largest number of high surface dust concentrations (Fig. 6c), and the March 9 case exhibited the lowest surface dust concentrations (Fig. 6a).

Retrievals of aerosol optical depth τ from the CIMEL sun photometer show maximum aerosol optical depths of approximately 0.4 on March 9 and March 15, and 0.45 on February 15 (Fig. 7a, b, c, respectively). The number of CIMEL τ retrievals is related to the presence of daytime clear-sky conditions; cloud cover was present over the site prior to 18:00 UTC on March 9, and there was

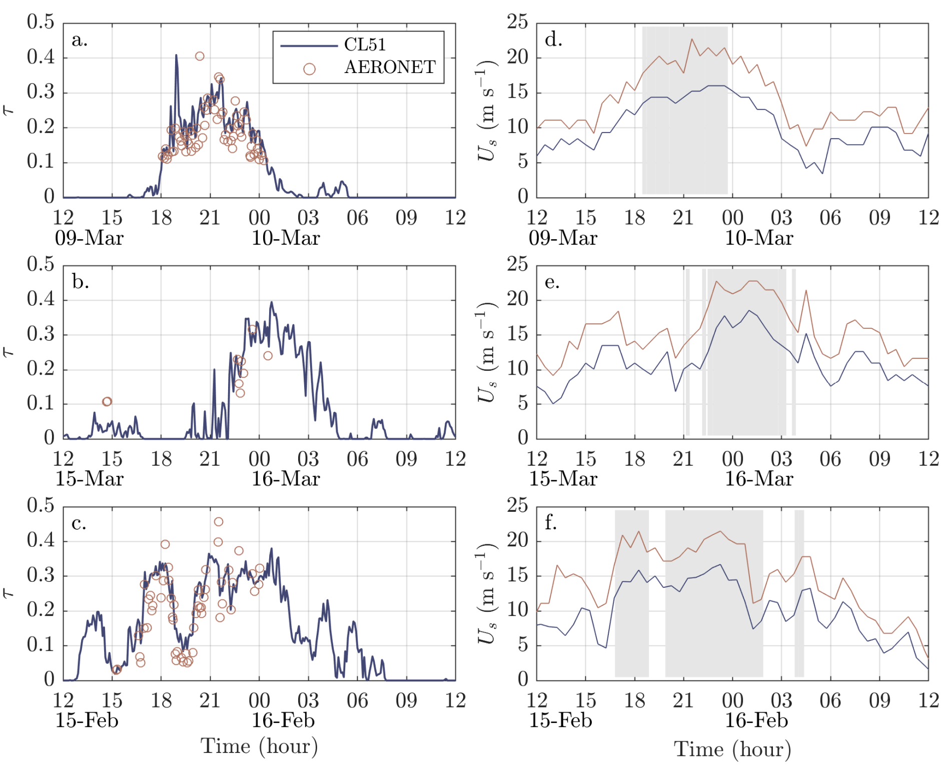

FIG. 7. Aerosol optical depth τ retrievals and surface wind speeds measured at the field site during the three dust cases. Shown in 7a–c are time series of τ retrieved from the CL51 (solid line) and the AERONET sun photometer (circles) during each of the three dust outbreaks. Shown in 7d–f are corresponding measurements of surface wind speeds (blue) and gusts (red-orange), with time periods during which $\tau \geq 0.2$ indicated by the gray shading.

intermittent cloud cover throughout the March 15 event, whereas the sky was clear on February 15 (see animations M1–3 in the Supplement). Post-processed values of τ retrieved from the CL51 are broadly in agreement with those from AERONET, and thus can be used to estimate τ in the subcloud layers and at nighttime. If we arbitrarily define a dust outbreak as $\tau \geq 0.2$, from these data the duration of the March 9 event was approximately 5 hours (Fig. 7a, 18:35 to 23:35 UTC), the March 15 event lasted 5.5 hours (Fig. 7b, 22:15 to 03:45 UTC), and the February 15 event had a duration of 11.17 hours (Fig. 7c, 17:05 to 04:15 UTC), although the latter event was punctuated by distinct periods of $\tau < 0.2$ at 15:00, 19:30, and 03:00 UTC.

A comparison of measurements of τ and the corresponding surface wind speed U_s suggests that, in general, $\tau \geq 0.2$ when the surface wind speeds and gusts exceed 9 and 17 m s^{-1}, respectively (gray shading in Figs. 7d–f). Although for the February 15 case there are several time periods during which $\tau > 0.2$ but wind speeds are well below 9 m s^{-1}, and when $\tau < 0.2$ but wind speeds are above 9 m s^{-1} (Fig. 7f). For these cases dust over the field site is emitted from the upwind desert region to the west (see animations M1–3 in the Supplement), and as discussed in Section 4, decoupling of τ and U_s in the February 15 case may be due to the influence of non-stationary trapped waves.

Measurements of backscatter made from the CL51 ceilometer located at the field site provide information about the vertical structure of the dust storms. Plotted in Fig. 8 are $\log_{10}$ of the ceilometer range corrected backscatter signal within the lower 4 km of the atmosphere for 24 hour periods commencing at 12:00 UTC on March 9 (Fig. 8a) and 15, 2021 (Fig. 8c) and February 15, 2022 (Fig. 8e). Values of $\log_{10}$ backscatter that are greater than 2 are a reasonable indication of the presence of suspended dust based on comparisons with aerosol optical depth retrievals from the collocated sun photometer (Evan et al. 2022a), and backscatter values greater than 2 that are located well above the surface indicated the presence of clouds (e.g., 2-3 km AGL at 20:00 UTC on March 15 in Fig. 8c).

The CL51 data show that for all three cases dust is confined to a layer below 2 km AGL, but that the depth of the dust plume and the vertical distribution of the aerosols vary both between events and within the individual dust outbreaks. For example, the dust outbreak on March 9 is characterized by a plume having depth 1-2 km AGL (Fig. 8a) with extinction values peaking at 500 m AGL (Fig. 8b). For the March 15 case dust is confined to the shallow layer of 300-700 m AGL (Fig. 8c), with extinction peaking at the lowest retrievable level of 100 m AGL (Fig. 8b). Differences in the shapes of the extinction profiles for the March 9 and 15 cases explain why surface PM_{10} measurements for the March 15 case were far greater than those for March 9 (Figs. 6a, b) although the dust optical depth for these two events are nearly identical in magnitude (Figs. 7a, b). The ceilometer data for February 15 exhibits distinct periods of dust layer depths, ranging from 600 m to 2 km AGL (Fig. 8e). We consider the factors affecting the vertical distribution of dust in Section 4.

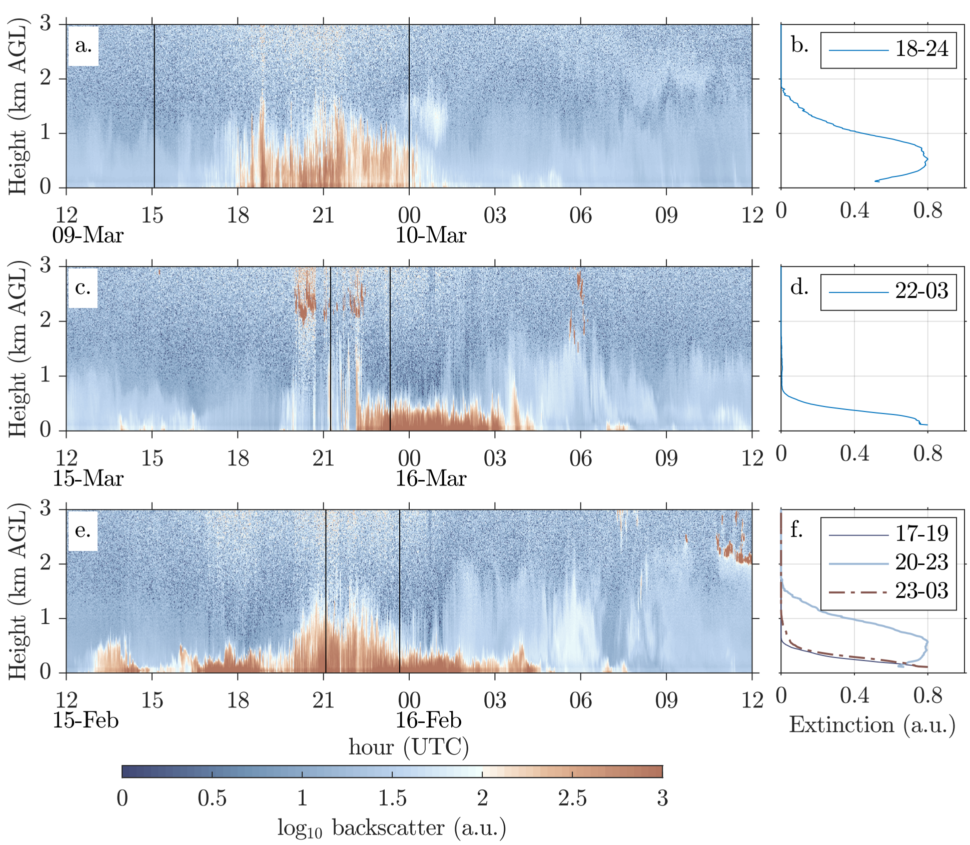

FIG. 8. Ceilometer backscatter and extinction profiles from CL51 measurements made at the field site. Shown are vertical profiles of the log of the CL51 range corrected signal during the dust outbreaks on March 9 & 10 (8a) and 15 & 16, 2021 (8c), and February 15 & 16, 2022 (8e). The vertical black lines in each represent times radiosondes were launched at the site (Fig. 9). Plotted in 8b, d, f are extinction profiles averaged over the time period indicated in the legends (in hours UTC), and corresponding to the days indicated in the adjacent panels.

c. Terrain Forced Flow

Having provided an overview of the synoptic situation for these dust events and examined the physical characteristics of the airborne dust, we next consider the role of orography in generating the high winds that gave rise to the dust outbreaks. The mountain range that lies immediately to the west of the Salton Basin (the Peninsular Mountains) is north-south oriented and rises gradually from the Pacific Ocean to peak heights up to 3 km, with steep eastern slopes that plunge into the sub-sea level Salton Basin (Fig. 1b, see also Fig. 5 in Evan 2019). Given the characteristics of the Peninsular Mountains (which hereafter we also refer to as the upwind barrier), wind in the zonal direction is cross-barrier and thus westerly flow has the potential to generate strong downslope windstorms in the lee of these mountains (Durran 1990). In order to elucidate the influence of the orography on the lee-side flow we examine radiosondes launched from the field site on each of the days in question and output from WRF simulations of these events.

A profile of potential temperature θ obtained from a radiosonde launched prior to the March 9 dust outbreak at 15:00 UTC (07:00 local time) shows the remnants of a nocturnal inversion, with θ increasing from 15 to 18 C from the surface to 1.5 km AGL, which is then capped by an approximately 4 C inversion layer, with θ increasing steadily above (Fig. 9a). The corresponding cross-barrier wind speeds u vary between 10 and 20 m s^{-1} throughout the lower 6 km of the atmosphere (Fig. 9b). A radiosonde released at 24:00 UTC on this day (16:00 local time), which is during the dust outbreak (Fig. 8a), shows 5 C warming at the surface relative to the 15:00 UTC sounding but little change in the 1-1.5 km layer. If we define the top of the convective boundary layer as the height at which θ equals the surface temperature, which is reasonable given that the layer is dry, the depth of the convective boundary layer during the dust outbreak is 1.5 km, which is consistent with the depth of the dust layer during this event (Fig. 8b).

During the March 9 dust outbreak the profile of u can be characterized as consisting of a low-level jet having peak wind speeds of 20 m s^{-1} from just above the surface to a height of 1 km AGL, and a wind speed minimum of 5 m s^{-1} at the height of the inversion at 1.5 km AGL (Fig. 9b). The height of the wind speed minimum and 4 C inversion are also located at a minima in the balloon's ascent rate, which is in contrast to the more constant ascent rate prior to the dust outbreak (Fig. 9c). Inversions apparent in the profile of θ at heights of 1.5, 3.5, and 4.9 km AGL are coincident with minima in ascent rate and thus the magnitudes of these inversions are affected by the reductions in the radiosonde's vertical velocity. Minima in the ascent rate also indicate the presence of waves, similar to cases examined in Strauss et al. (2016). The presence of waves is also apparent in measurements from other soundings made during these events (Figs. S6, S12).

Radiosondes launched immediately prior to and during the dust outbreak on March 15, 2021 show some similar characteristics to those from the March 9 case. The vertical profile of θ prior to the dust outbreak at 21:15 UTC (14:15 local time, Fig. 8c) suggests a well-mixed boundary layer extending from the surface to approximately 2 km AGL (Fig. 9d) with u near 10 m s^{-1} throughout this depth (Fig. 9e). In contrast, the sounding made during dust outbreak (23:20 UTC, 16:20 local time) is accompanied by cooling of approximately 3 C in the lower 500 m of the atmosphere (Fig. 9d) and a pronounced low level jet characterized by peak wind speeds of 23 m s^{-1} at heights of 100-300 m AGL and a wind speed minimum of 5 m s^{-1} at 1.25 km AGL. The radiosonde ascent

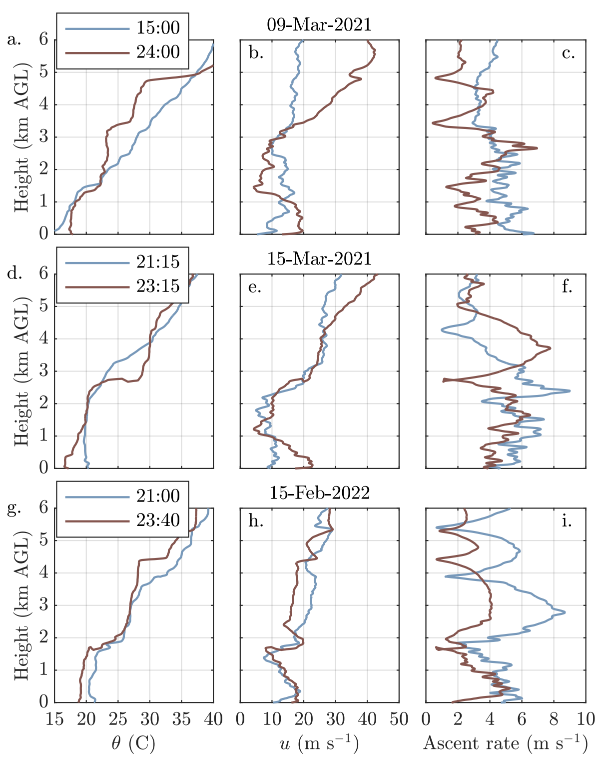

FIG. 9. Sounding measurements from radiosondes launched from the field site on March 9 2021 (9a–c), March 15 2021 (9d–f), and February 15 2022 (9g–i). Plotted are radiosonde profiles of potential temperature θ (9a,d,g), zonal wind speed u (9b,e,h), and balloon ascent rate (9c,f,i). Times of the radiosonde launches (UTC hours) are indicated in the legends in 9a,d,g.

rates implies wave activity in the atmosphere, with a minimum in ascent rate at 2.8 km AGL (Fig. 9f) that is located at the height of a nearly 10 C inversion (Fig. 9d). We again note that this apparent inversion is heavily influenced by the nearly horizontal motion of the balloon at this height.

The low-level cooling accompanying the onset of high wind speeds helps explain the observed shallow depth of the dust layer on March 15, relative to the March 9 case (Fig. 8d). These features of the March 15 dust outbreak are similar to those for a dust outbreak that occurred on February 22, 2021, which was generated by spillover precipitation and evaporative cooling over the desert to the west of the research site (Evan et al. 2022c). Here we noted no spillover precipitation for the March 15 case and thus any density-current like features are due to cold post-frontal downslope flow (Karyampudi et al. 1995; Koch et al. 1991).

For the February 15, 2022 case no radiosondes were launched prior to the dust outbreak, although the radiosondes measurements shown in Figs. 9g–l do correspond to periods of differing heights of the dust plume (Fig. 8e). Profiles of potential temperature made at 21:00 UTC (13:00 local time) and 23:40 UTC (15:40 local time) show an inversion just below 2 km AGL (Fig. 9g). For the earlier time we estimate a convective boundary layer depth of 1.6 km, which is consistent with the depth of the dust layer averaged from 20:00-23:00 UTC (Fig. 8f). For the 23:40 sounding there is relative cooling of approximately 1.5 C in the lower 1.8 km of the atmosphere, and 2.0 C at the surface. This change in the θ profile suggests that the depth of the convective boundary layer is reduced to 1 km AGL, consistent with the depth of the dust layer averaged from 23:00-03:00 UTC (Fig. 8f).

Similar to the March 9 and 15 cases, zonal wind speeds from radiosondes launched during the dust outbreak on February 15 show low level jets, with speed maxima of 18 m s^{-1} located at heights of 400-500 m AGL, and wind speed minima of 8 m s^{-1} at 1.5-1.75 km AGL (Fig. 9j). For these cases we also find minima in radiosonde ascent rates that are coincident with inversions present in the θ profiles, including at 1.9, 3.9, and 5.4 km AGL for the 21:00 UTC sounding (13:00 local time), and 1.7, 4.5, and 5.3 km AGL at 23:40 UTC (15:40 local time, Fig. 9k), again reflecting the presence of waves in the overlying atmosphere.

We again utilize radiosondes made from the NKX sounding station located near the coast (Figs. 1, 3) in order to understand the factors that give rise to these downslope windstorms via examination of radiosondes released at 24:00 UTC from this location and the nearest in time radiosondes released from the field site near the Salton Sea (Fig. 10). According to Mayr and Armi (2010) lee-side flow will plunge to the floor of the basin if the potential temperature of the air flowing over the ridge is cooler than that of the down-barrier surface. The heights of the ridgeline upwind of the field site are in the range of 1.25 to 1.75 km AMSL (gray shaded band in Fig. 10), and the upwind (NKX) potential temperatures at these heights (Figs. 10a–c, light-blue) are all lower than the downwind values of θ below 1.25 km (Figs. 10a–c, rust). Vertical profiles of wind speed from the NXK soundings suggest upwind orographic flow blocking, as evidenced by wind speeds below 1.25 km in the range of 5-12 m s^{-1} that are in contrast to the high wind speeds downwind of the barrier (Figs. 10d–f). Above the heights of the ridge the upwind and downwind wind speed profiles are similar, with the exception of the jet at 1.75-2.5 km in the February 15 downwind profile (Fig. 10f), which is due to the influence of wave activity on the radiosonde ascent rate. These differences in the soundings upwind and downwind of the barrier are consistent with isentropic drawdown of the

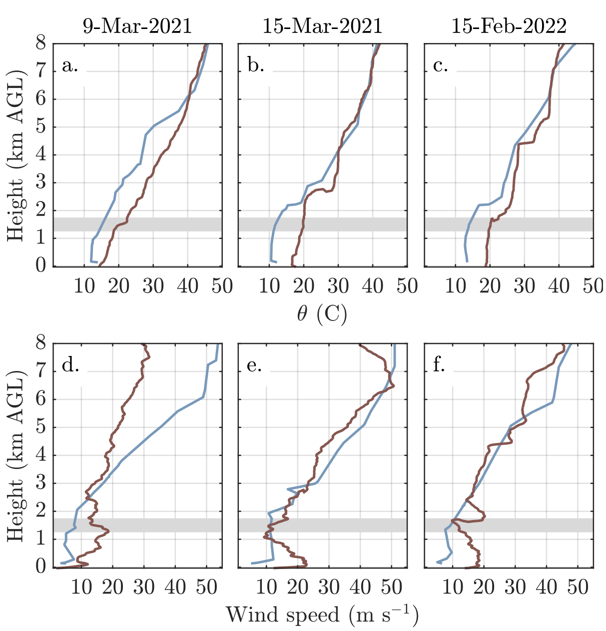

FIG. 10. Radiosonde profiles of θ (top row) and wind speed (bottom row) from San Diego, CA (NKX), which is upwind of the barrier (light-blue) and from the field site that is located near the Salton Sea (rust). The heights of the mountain ridge represented by the gray shaded band in each panel. Profiles are shown for the 24:00 UTC soundings from San Diego and the radiosondes launched closest to this time near the Salton Sea (i.e., the later sounding times in Fig. 9) for March 9 (10a,d) and March 15, 2021 (10b,e), and February 15, 2022 (9c,f).

cross-barrier flow at or above the the height of the ridgeline and a lee-side downslope windstorm Durran (1990).

d. Numerical Simulations with WRF

In order to provide broader context to the in-situ measurements we also examine output from numerical simulations using WRF, focusing on model output along the 33.25°N latitude transect for the innermost model domain (Fig. 2). The WRF simulations reproduced several aspects of the surface and upper air measurements, including strong westerly surface wind speeds during the dust events (Fig. S1). However, at least at the field site, the simulated timing of the onset and termination of high wind speeds did not line up with observations, and for several cases waves in

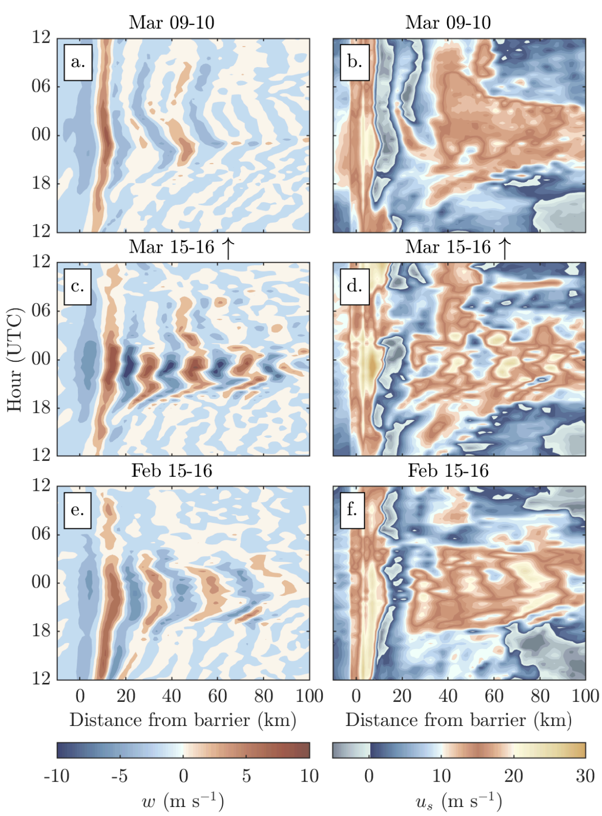

FIG. 11. Hovmöller diagrams of 3-4 km height averaged vertical velocity w (11a,c,e) and surface zonal wind speed u_s (11b,d,f) along the 33.25°N latitude transect during the March 9 2021 (11a–b), March 15 2021 (11c–d), and February 15 2022 (11e–f) dust outbreaks. The upward pointing arrows in 11a,b indicate the location of the field site. Reference orography along this transect can be found in Fig. 12.

the model appeared to be out of phase with wave activity implied by changes in the radiosonde ascent rate (Figs. S2–S13). As such, WRF output is used to understand the general behaviour of the downslope flow and trapped waves in the Salton Basin, rather than to explain the timing of specific aspects of these events.

Hovmöller diagrams of vertical velocity w averaged over the 3-4 km layer during 24-hour time periods starting at 12:00 UTC on March 9 (Fig. 11a) and March 15, 2021 (Fig. 11c), and February 15, 2022 (Fig. 11e) indicate the presence of trapped lee waves during the periods of observed high winds and dust (Fig. 7). For all three cases and during the entire 24-hour time period downslope flow is simulated along the lee side slopes of the upwind barrier (the barrier ridge is located at the 0 km point on the horizontal axis and flow downwind of the barrier is located at positive horizontal distances, a transect of the orography is found in Fig. 12), and then vertical ascent at 10 km distance from the barrier. This type of plunging flow and downwind jump has been the focus of research on high wind events and dust storms in the Owen's valley (e.g., Grubišić et al. 2008). Indeed, similarly constructed Hovmöller diagrams of u at the lowest model level indicate the strongest surface winds ($u > 20$ m s^{-1}) along the lee-side slopes for all three cases (Figs. 11b,d,f). However, distinct from the narrow Owen's valley, in the Salton Basin the terrain of the first 35 km downwind of the barrier is vegetated and generally non-emissive, and as such the high winds associated with the flow at the base of the barrier do not produce dust here.

A distance-height transect of model output vertical velocity w (Figs. 12a,d,g) and dry isentropes (Figs. 12b,e,h), averaged over two-hour time periods during which the waves are approximately stationary, indicate the existence of trapped waves in all three cases. The weakest wave activity is seen in the WRF output for March 9, where the magnitude of the vertical wind speeds drop below 1 m s^{-1} at a distance of approximately 60 km from the mountain ridge (Fig. 12a). The March 15 case exhibits the strongest wave activity, with waves of quasi-regular wavelength 20 km and vertical velocity magnitudes as large as 5 m s^{-1} at a barrier distance of 85 km (Fig. 12d). The February 15 case also shows strong wave activity throughout the model domain, but of smaller magnitude and longer wavelength than that for March 15 (Figs. 12g). For all three cases the waves are evanescent above approximately 6 km height (Fig. 12b,e,h), due to changes in static stability and vertical wind shear in the flow upstream of the orography (Fig. 10).

Relevant to understanding the influence of trapped waves on dust emission and transport is their effect on surface wind speed u_s. Firstly, from the Hovmöller diagrams in Fig. 11 the strongest wind speeds are in-general found along the leeside slopes, with weak and even reversed flow just downwind of the barrier base, indicative of flow separation and a rotor circulation (Doyle and Durran 2002). Further downwind of the barrier the strongest surface wind speeds ($u_s > 20$ m s^{-1}) are associated with the presence of trapped waves. For example, in the February 15 case plunging

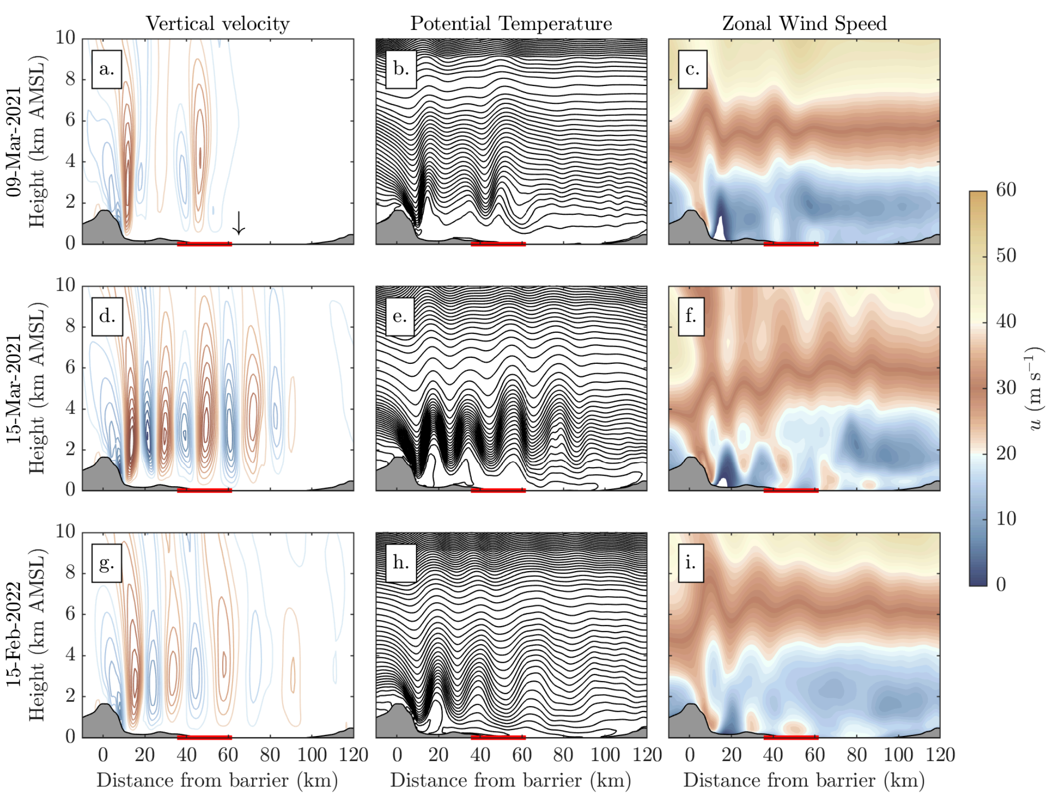

FIG. 12. WRF output along the 33.25°N latitude transect averaged over simulation times 21:00-23:00 UTC on March 9, 2021 (12a–c), 22:00–24:00 UTC on March 15, 2021 (12d–f), and 22:00–24:00 UTC on February 15, 2022 (12g–i). Horizontal distance is given in km from the peak of the upwind ororgraphy. Plotted in 12a,d,g are vertical wind speeds w in contour intervals of 1 m s^{-1}, with warm colors representing positive w and cool colors representing negative w, and where the 0 m s^{-1} isotach is not plotted. Plotted in 12b,e,h are lines of constant θ in 1 C intervals. Shown in 12c,f,i is u, where the white shaded region at the downwind base of the orography indicates reversed flow ($u < 0$). The downward pointing arrow in 12a represents the location of the field site. The red horizontal line in all figure panels represents the approximate locations of dust emission that are upwind of the field site.

flow along the lee-side slopes (0-10 km) produce horizontal surface wind speeds near 30 m s^{-1} from 12:00–00:00 UTC (Fig. 11f). Prior to the development of trapped waves at approximately 18:00 UTC (Fig. 11e) surface wind speeds at barrier distances greater than 20 km are below 10 m s^{-1}. As lee waves develop surface wind speeds greater than 25 m s^{-1} are found as far as 90 km from the barrier. In general and for these cases, since dust emission primarily occurs at barrier distances greater than 35 km, significant dust uplift in the basin would only occur after lee wave onset.

The effect of wave activity on surface wind speed u_s is apparent in the cross-sections of zonal wind speed (Fig. 12c,f,i). Perturbations in u_s are out of phase with horizontal gradients in w and are in phase with θ, which is due to surface pressure minima under the regions of strongest upward vertical velocity, and surface pressure maxima located under the strongest downdrafts (Nappo 2013). For all three cases the strongest surface wind speeds are all found under the wave troughs. Although the speed of the plunging flow along the lee side slopes is very similar for all three cases, surface wind speeds further downwind of the barrier (distances greater than 20 km) are the weakest in the March 9 case, in which the trapped waves are less pronounced and dissipate at barrier distances greater than 50 km, and are the strongest downwind during the March 15 case, in which the waves are still coherent at barrier distances greater than 80 km.

4. Discussion

Orographically forced waves can become trapped in a layer near the surface if the static stability or curvature of the wind shear change with height such that waves cannot propagate upward and are thus evanescent with height. Wave trapping can be predicted by vertical changes in the Scorer parameter l^2 upwind of the barrier, which is defined as (Scorer 1949)

$$l\,(z)^2 = \frac{N^2}{\bar{u}^2} - \frac{1}{\bar{u}}\frac{d^2\bar{u}}{dz^2} \tag{1}$$

where $\bar{u}$ indicates the cross-barrier wind speed and N the Brunt-Vaisala frequency, both of which are resolved in z. For example, if we consider the atmosphere to consist of uniform lower and upper layers, orographically forced gravity waves become trapped in the lower level for

$$l_L^2 > k^2 > l_U^2$$

where k is the horizontal wavenumber of the trapped waves and l_L^2 and l_U^2 are Scorer parameters of the lower and upper layers, respectively. For the idealized case of constant wind speed with height in the upwind atmosphere these conditions are satisfied if N^2 of the upper layer is less than that of the lower layer, meaning that the buoyancy restoring force in the upper layer N_U^2 is too weak to support gravity waves for which $k^2 > N_U^2/\bar{u}^2$. Thus wave energy remains trapped in the lower layer.

Plots of l^2 for the 24:00 UTC soundings made upwind of the barrier at the NKX site (see location in Fig. 1) show a reduction in l^2 with height for all three cases (Fig. 13). For March 9, l^2 peaks low

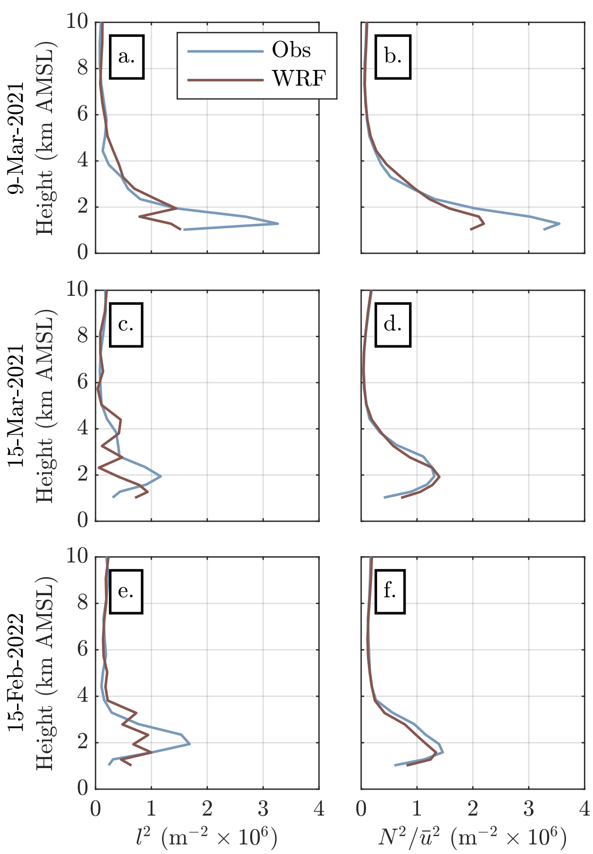

FIG. 13. Changes in the Scorer parameter with height. Plotted in the left-hand column panels is the Scorer parameter l^2 (Eq. 1) calculated from the 24:00 UTC soundings made from the NKX station (blue) and output from the WRF simulations (rust), for the dates indicated at left. Plotted in the right-hand columns is the l^2 stability term (first term on the right-hand-side of Eq. 1), for the same data. Only values above 1 km are shown due to the blocked flow below this height (e.g., Fig. 10).

in the atmosphere, at a height of 1.3 km (Fig. 13a) and reaches a minimum at 4 km. For the other two cases l^2 peaks slightly higher in the atmosphere at 2 km, and reaches a minimum at 5.8 km (Fig. 13c) and 4.5 km (Fig. 13e). Profiles of the first term on the right-hand-side of Eq. 1 suggest that variations in l^2 are primarily driven by reductions in static stability above 2 km (Fig. 13b, d, f), since in all three cases $\bar{u}$ increases nearly monotonically with height above the barrier (Fig. 10d–f).

In the model the reductions in l^2 with height are not as large as in the observations (Fig. 13a,c,e). This difference is due to discrepancies between the observed and simulated shear profiles as there is generally good agreement in the l^2 stability terms. We note that for the March 9 case the modeled stability term does not drop off as strongly with height as does that from observations (Fig. 13b), and thus it is plausible that the model is under predicting trapped wave activity for the three cases considered here.

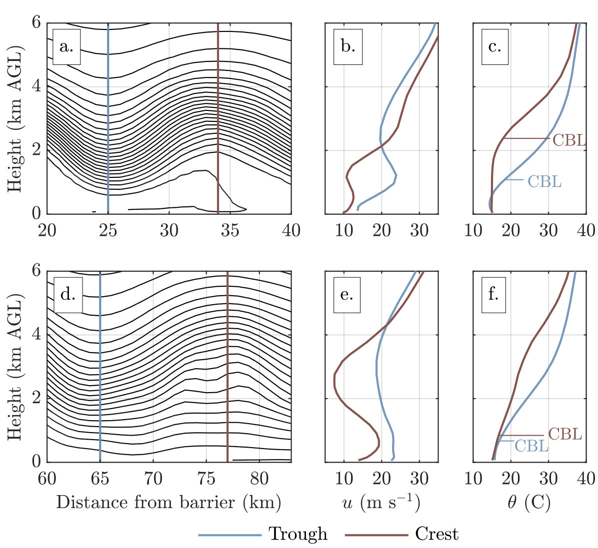

FIG. 14. Changes in model zonal wind speed u and potential temperature θ with height for different wave phases and proximity to the surface. Plotted in 14a and 14d are contours of isentropic surfaces at 1 C intervals from the WRF output shown in Fig 12e (March 15, 2021 case) at barrier distances of 20-40 km (14a) and 60-83 km (14f), where the vertical blue and rust colored lines in 14a,d indicate the locations of the wave troughs and ridges used to generate the profiles in the other figure panels. In 14b,e are profiles of cross-barrier wind speed u corresponding to the wave troughs (blue) and ridges (rust). Descriptions of the plots in 14c,f are the same as for 14b,e except that θ is plotted, and where the horizontal lines indicate the model-calculated height of the convective boundary layer (CBL).

Based on the measurements and model output presented here we suggest several characteristics of dust storms generated by trapped waves. The first is the presence of a low-level jet (Fig. 10d–f), which is relevant in terms of dust production, advection, and dispersion due to the strong wind speeds characterizing the jet, and the potential for enhanced turbulence production in the shear zones above and below the jet nose. Pressure perturbations associated with wave phase generate positive and negative horizontal wind speed perturbations under the wave troughs and crests, respectively (Durran 1986), resulting in vertical profiles of horizontal wind speeds u that resemble a low level jet at the base of the wave trough or at the surface under a wave crest. The effect of wave phase on vertical profiles of wind speed can be readily seen in the output from the WRF simulations for the March 15 case (Fig. 12d–f), averaged from 22:00–24:00 UTC. Focusing on one cycle of the simulated wave over barrier distances of 20-40 km (Fig. 14a), the simulated zonal (i.e., cross-barrier) wind speed u is stronger under the wave crest than under the trough, from the surface up to a height of 2 km AGL (Fig. 14b), which is the height where the isentropes above the trough start to spread vertically. Under the wave trough u increases by 10 m s^{-1} from the surface to the base of the wave at 1 km AGL. Under the crest there is a local maximum in u at approximately 500 m AGL above which u decreases by 2 m s^{-1} to the local minimum at 1.3 km AGL. As such, the low-level jet under the wave trough is more pronounced than that for the crest and has a nose located at the base of the wave, while that under the crest is weaker with a nose located close to the surface.

For the same WRF simulation but at barrier distances of 60-83 km (Fig. 14d), possibly more representative of the environment over the field site, the simulated wave is evanescent to the surface. Here u is greater under the wave trough than the crest up to a height of 4 km AGL (Fig. 14e), which for the trough is the height above which the isentropic surfaces start to spread vertically. While there is no obviously discernible low-level jet under the wave trough, under the crest there is a greater than 10 m s^{-1} reduction in u from the local maximum at 500 m up to the minimum at 2.5 km AGL, above which the isentropes become more tightly packed, signifying the wave base. The similarity between the low-level jet under the wave crest in Fig. 14e and the wind speed profiles in the soundings made during the dust outbreaks (Fig. 9b,e,h) raise the possibility that the site is often located under wave crests during trapped wave events.

We suggest that another characteristic of dust storms generated by trapped lee waves is the variable convective boundary layer and thus dust layer depths, which are dependant upon the phase and proximity to the surface of the overlying wave. Returning to the WRF output from the March 15 case and barrier distances of 20-40 km (Fig. 14a), under the wave trough isentropes are displaced downwards towards the surface, resulting in a modeled boundary layer height of 1 km AGL (Fig. 14c). In contrast, under the wave crest isentropic surfaces are displaced upwards such that θ is little changed from the surface up to nearly 2 km AGL, with a corresponding boundary layer height of 2.4 km AGL. When considering distances of 60-83 km from the barrier (Fig. 14d) there is little difference in the vertical distribution of θ under the wave trough and crest in the lower 1 km of the atmosphere due to the proximity of the wave to the surface, with each exhibiting similar boundary layer heights of 0.7 and 0.8 km AGL, respectively (Fig. 14f), which are more shallow than those for the previous case. The relatively shallow simulated boundary layers in Fig. 14f may explain why for the three cases considered here the observed dust layer depths are shallow (Fig. 8), and the surface PM_{10} concentrations are high (Fig. 6).

We further consider the effect of wave phase on dust layer depth via simulations with WRF-Chem. A transect of dust concentration from WRF-Chem for the March 15 case at 23:30 UTC and for the first 70 km downwind of the barrier indicates that the depth of the dust layer closely follows the curvature of the isentropic surfaces that define trapped wave base (Fig. 15a). Furthermore, the highest dust concentrations are found under the wave crests, where the simulated zonal and cross-barrier wind speeds are near zero or negative (Fig. 12f) and the boundary layer turbulent kinetic energy is large (not shown), implying that the areas under the wave crests are regions of strong vertical diffusion and weak down-barrier transport of dust, explaining why the isopleths of high dust concentrations (e.g., > 0.2 mg m^{-3}) increase with barrier distance.

A map of the horizontal structure of dust mass path, which is the vertically integrated concentration, also for 23:30 UTC on this date (Fig. 15b) shows coherent northwest-southeast oriented wave fronts of high and low dust mass path that closely follow the orientation of the upwind topography. As such, in addition to depth of the dust layer, trapped waves have a strong effect on the horizontal distribution of dust concentration. A map of the corresponding surface dust emission flux (Fig. 15c) does not clearly show any resemblance to the structure of the waves, owing to the dominant influence of surface characteristics on dust emission, suggesting that the spatial structures of dust concentration and mass path are largely the result of advection and diffusion rather than the spatial pattern of emission. We also note that under the wave crests the cross-barrier wind speeds are weak but the along-barrier wind speeds are northerly (not shown), raising the possibility of meridional dust advection there.

We again note that while these WRF-Chem simulations are useful in terms of elucidating the general characteristics of dust storms generated by trapped waves, they are of limited use in terms

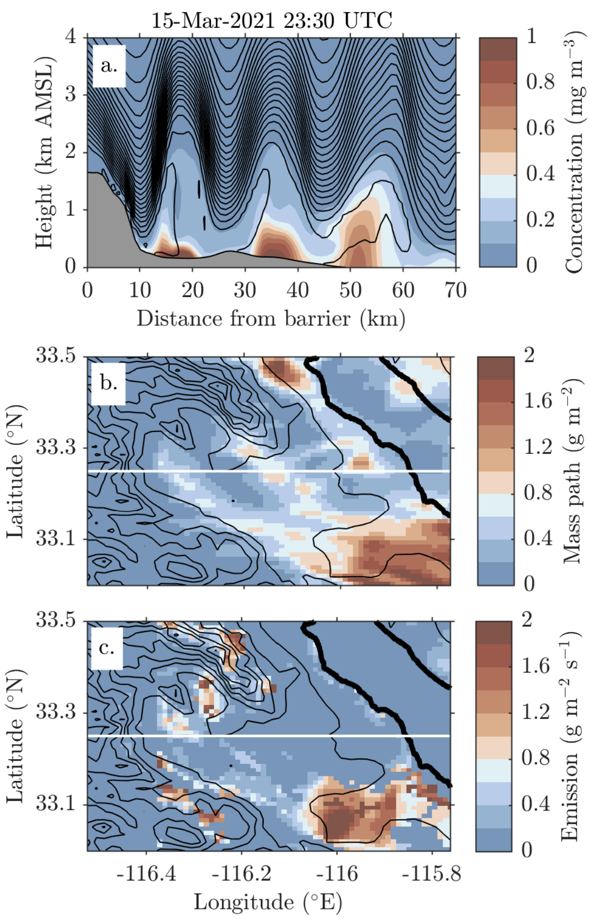

FIG. 15. Dust simulated by WRF-Chem at 23:30 UTC on March 15, 2021. In 15a are isentropic surfaces at 1 C intervals (contours) and dust concentration (mg m^{-3}) along the 33.25°N a zonal transect, in km downwind of the barrier crest. In 15b is the horizontal distribution of dust mass path (g m^{-2}) along the transect in 15a but in zonal units of °E. Black contour lines indicate topography intervals of 250 m, the thick black line indicates the Salton Sea shoreline, and the white horizontal line the latitude of the transect in 15a. The description for 15c is the same as for 15b except that average dust emission over the preceding 30 min (g m^{-2} s^{-1}) is shown.

of understanding the specific distribution of dust in the region during these events. Eyewitness accounts and GOES-R and Roundshot camera animations (M1–M3 in the Supplement) show that during these events dust is mainly emitted from the low-lying desert regions (i.e., barrier distances greater than 40 km in Fig. 15a) whereas the model shows little to no emission in this area (Fig. 15c, -116.2 to -116°E and 33.2 to 33.3°N). Ongoing work suggests that apparent unrealistic distribution of dust emission is at least in part due to erroneous land surface type classification.

Lastly, our results imply that a third characteristic of dust storms generated by trapped waves is that wave-forced wind speed perturbations, and thus dust emission, can occur far downwind of the barrier. Output from the WRF simulations indicate that surface wind speed perturbations associated with trapped waves occur as far as 100 km downwind of the barrier (Figs. 11, 12). Radiosondes also indicate the presence of waves downwind of the field site during all three cases (Fig. 9), where plots of balloon height and ascent rate as a function of zonal distance from the field site imply that waves are found at barrier distances greater than 100 km (e.g., Figs S6, S8, S13).

Wave-forced wind speed perturbations are also likely to have a large impact on dust emission given the power law relation between emission and surface wind speed (e.g., Kok et al. 2014). For example, we consider two idealized cases of downslope windstorms, in which the surface wind speed of the first is constant with barrier distance $u_1(x) = c_1$, and the surface wind speed of the second is sinusoidal about the same mean $u_2(x) = c_1 + c_2 \cos(x)$, a simplification of wind speed perturbations due to the influence of overlying trapped waves. Evoking the dust uplift potential approximation to the relationship between emission and surface wind speed (Marsham et al. 2011) and assuming wind speeds of sufficient magnitude to loft dust, in either case the total dust emission E over a non-dimensionalized distance 2π is

$$E \propto \int_0^{2\pi} u(x)^3$$

so that the total emission for the second case E_2 can be expressed as a function of the first case E_1,

$$E_2 = E_1 + 3\pi c_1 c_2^2$$

where it is implied that the second term is multiplied by some positive constant of proportionality. Thus, there is a larger net flux of dust into the atmosphere for the second case, and this relative increase in emission is proportional to the product of the mean wind speed c_1 and the square of magnitude of the perturbations c_2.

5. Conclusion

Observations of three dust outbreaks that occurred in the northwestern Sonoran Desert indicated that these storms were all associated with the presence of trapped lee waves generated by a north-south oriented mountain range. Reanalysis demonstrated that for each case cross-barrier flow was directed over the region by way of a synoptic scale low pressure trough transitioning through the area (Fig. 3). Surface meteorological measurements showed that during trough passage flow over a field site located near the western shoreline of the Salton Sea (Fig. 1) was westerly with wind speeds and gusts exceeding 10 and 20 m s^{-1}, respectively (Fig. 5). Measurements of PM_{10} (Fig. 6) and animations from a Roundshot camera and GOES-17 (Supplemental Materials M1–M3) indicated the presence of dust across the region, and aerosol optical depth retrievals from a sun photometer and a ceilometer exhibited values greater than 0.3 during the dust outbreaks. Backscatter profiles from the ceilometer suggested that the depths of the dust layers ranged from 700 m to 2 km (Fig. 8). Radiosondes released prior to and during the dust events suggested that the high winds were associated with a shallow convective boundary layer, one factor in generating the shallow dust layers, and the presence of a jet in the lower 1.5 km of the atmosphere (Fig. 9). Radiosonde ascent rates implied the presence of trapped waves in the environment downwind of the field site (Figs. 9, S6, S8, S10—13), consistent with numerical simulations conducted with the WRF model showing that each of the dust-producing high wind events were at some point associated with the presence of trapped lee waves (Fig. 11), resulting in positive surface wind speed perturbations far downwind of the wave-generating barrier (Fig. 12).

We highlighted several meteorological aspects of the observed and simulated trapped waves that are relevant to understanding the characteristics of the concurrent dust outbreaks. These include the presence of a low level jet whose depth and speed is affected by wave phase and vertical structure, dust layer depths and concentrations that are also dependent upon these factors, and high wind speeds and dust emission more than 100 km downwind the wave source. Output from WRF-Chem provided corroborating evidence that the depth of the dust layer is strongly tied to wave phase, with the model showing the highest dust concentrations under the wave crests. Direct observational evidence to evaluate many aspects of the wave-forced dust storm characteristics (e.g., the relationship between wave phase and depth of the dust layer) would require measurements of aerosols and meteorology at different wave phases and at concurrent times, something that is not currently possible given the available instrumentation at this single field site.

Inversions upwind and near the heights of the ridge of the Peninsular Mountains were noted for the March 15 2021 and February 15 2022 cases (Fig. 10), as well as in the cases examined in Evan et al. (2022c) and Evan (2019). As such, trapped waves are likely a common feature of strong cross barrier flow and dust outbreaks in the region. Observations and modeling from the Owen's valley suggest, however, that the Salton Sea is not unique in this regard (e.g., Grubišić and Billings 2007). More work to evaluate the role of trapped waves on dust emission in other dust-emitting regions is warranted, especially since climate models do not directly simulate nor parameterize trapped waves.

The Salton Sea is rapidly drying, and thus the area of exposed playa and potential for increasing dust emission is growing. The Salton Sea sits immediately downwind of the field site, and as such trapped waves have the ability to generate high wind speeds and dust over the growing playa surfaces. It is not clear how the drying of the sea and the resultant changes in the surface temperature and sensible and latent heat fluxes will feedback onto wave activity. It is possible that a warming surface will heat the overlying atmosphere resulting in a reduction of wave amplitude (Jiang et al. 2006), although this effect could also increase the strength of the surface winds by allowing isentropes at the barrier level to more frequently reach the downwind surface. It is also unknown how drying of the sea may affect the depth of the dust layer; while increased surface heating implies a deeper convective boundary layer, the interaction of surface warming with wave activity may increase the near surface stability. It is also plausible that radiative heating by the dust will in-turn feedback onto the wave characteristics. Given the rapid environmental change occurring in this region and the health impacts of exposure to dust on the community (Frie et al. 2017, 2019; Jones and Fleck 2020; Biddle et al. 2022), more work to elucidate the impacts of the drying Salton Sea on the region's meteorology and air quality is warranted.

Acknowledgments. Funding for this work was provided by NSF Award AGS-1833173. We thank Trinity Robinson and Tyler Barbero for their assistance on this project, and three anonymous reviewers for their comments on a previous version of this manuscript.

Data availability statement. Salton Sea AERONET data is available via `aeronet.gsfc.nasa.gov/`, surface synoptic station data is at `mesowest.utah.edu/`, GOES-17 satellite data is at `www.avl.class.noaa.gov`, NEXRAD data is at `mesonet.agron.iastate.edu`, surface PM_{10} measrurements are from `www.arb.ca.gov/aqmis2/aqdselect.php`, NARR output is availiable from `psl.noaa.gov`, and GFS analysis is available from `www.nco.ncep.noaa.gov/pmb/products/gfs/`. The soundings, surface meteorological data, and CL51 backscatter and extinction profiles used in this manuscript are permanently archived at `https://doi.org/10.6075/J0BV7GTC` (Evan et al. 2022b).

References

Biddle, T., R. Chakraborty, Q. Li, M. Maltz, J. Gerrard, D. Lo, and Coauthors, 2022: The drying salton sea and asthma: A perspective on a "natural" disaster. *California Agriculture*, **76 (1)**, 27–36, https://doi.org/10.3733/ca.2022a0003.

Biddle, T. A., and Coauthors, 2021: Salton sea aerosol exposure in mice induces a pulmonary response distinct from allergic inflammation. *Science of The Total Environment*, 148450, https://doi.org/10.1016/j.scitotenv.2021.148450.

Buck, B. J., J. King, and V. Etyemezian, 2011: Effects of salt mineralogy on dust emissions, salton sea, california. *Soil Science Society of America Journal*, **75 (5)**, 1971–1985, https://doi.org/10.2136/sssaj2011.0049.

Burr, A. C., and Coauthors, 2021: Lung inflammatory response to environmental dust exposure in mice suggests a link to regional respiratory disease risk. *Journal of Inflammation Research*, **14**, 4035, https://doi.org/10.2147/JIR.S320096.

Chen, and J. Dudhia, 2001: Coupling an advanced land surface–hydrology model with the penn state–ncar mm5 modeling system. part i: Model implementation and sensitivity. *Monthly Weather Review*, **129 (4)**, 569–585, https://doi.org/10.1175/1520-0493(2001)129<0569:CAALSH>2.0.CO;2.

Chen, S.-H., and W.-Y. Sun, 2002: A one-dimensional time dependent cloud model. *Journal of the Meteorological Society of Japan*, **80 (1)**, 99–118, https://doi.org/10.2151/jmsj.80.99.

Chin, M., R. B. Rood, S.-J. Lin, J.-F. Müller, and A. M. Thompson, 2000: Atmospheric sulfur cycle simulated in the global model gocart: Model description and global properties. *Journal of Geophysical Research: Atmospheres*, **105 (D20)**, 24 671–24 687, https://doi.org/10.1029/2000JD900385.

Choobari, O. A., P. Zawar-Reza, and A. Sturman, 2014: The global distribution of mineral dust and its impacts on the climate system: A review. *Atmospheric Research*, **138**, 152–165, https://doi.org/10.1016/j.atmosres.2013.11.007.

De Wekker, S. F., and S. D. Mayor, 2009: Observations of atmospheric structure and dynamics in the owens valley of california with a ground-based, eye-safe, scanning aerosol lidar. *Journal of applied meteorology and climatology*, **48 (7)**, 1483–1499, https://doi.org/10.1175/2009JAMC2034.1.

Doyle, J. D., and D. R. Durran, 2002: The dynamics of mountain-wave-induced rotors. *Journal of the Atmospheric Sciences*, **59 (2)**, 186–201, https://doi.org/10.1175/1520-0469(2002)059<0186:TDOMWI>2.0.CO;2.

Durran, D. R., 1986: Another look at downslope windstorms. part i: The development of analogs to supercritical flow in an infinitely deep, continuously stratified fluid. *Journal of Atmospheric Sciences*, **43 (21)**, 2527–2543, https://doi.org/10.1175/1520-0469(1986)043<2527:ALADWP>2.0.CO;2.

Durran, D. R., 1990: Mountain waves and downslope winds. *Atmospheric processes over complex terrain*, Springer, 59–81, https://doi.org/10.1007/978-1-935704-25-6_4.

Durran, D. R., 2003: Lee waves and mountain waves. *Encyclopedia of atmospheric sciences*, **1161**, 1169.

Evan, A., B. Walkowiak, and R. Frouin, 2022a: On the misclassification of dust as cloud at an aeronet site in the sonoran desert. *Journal of Atmospheric and Oceanic Technology*, **39 (2)**, 181–191, https://doi.org/10.1175/JTECH-D-21-0114.1.

Evan, A. T., 2019: Downslope winds and dust storms in the salton basin. *Monthly Weather Review*, **147 (7)**, 2387–2402, https://doi.org/10.1175/MWR-D-18-0357.1.

Evan, A. T., C. Flamant, M. Gaetani, and F. Guichard, 2016: The past, present and future of african dust. *Nature*, **531 (7595)**, 493–495, https://doi.org/10.1038/nature17149.

Evan, A. T., R. Frouin, A. Kuwano, T. W. Barbero, T. Robinson, and S. R. Wynn, 2022b: Data from: The characteristics of dust storms generated by trapped waves in the lee of mountains. https://doi.org/10.6075/J0BV7GTC.

Evan, A. T., W. Porter, R. Clemesha, A. Kuwano, and R. Frouin, 2022c: Measurements of a dusty density current in the western sonoran desert. *Journal of Geophysical Research: Atmospheres*, e2021JD035830, https://doi.org/10.1029/2021JD035830.

Fast, J. D., W. I. Gustafson Jr, R. C. Easter, R. A. Zaveri, J. C. Barnard, E. G. Chapman, G. A. Grell, and S. E. Peckham, 2006: Evolution of ozone, particulates, and aerosol direct radiative forcing in the vicinity of houston using a fully coupled meteorology-chemistry-aerosol model. *Journal of Geophysical Research: Atmospheres*, **111 (D21)**, https://doi.org/10.1029/2005JD006721.

Fernald, F. G., 1984: Analysis of atmospheric lidar observations: some comments. *Applied Optics*, **23 (5)**, 652–653, https://doi.org/10.1364/AO.23.000652.

Field, J. P., and Coauthors, 2010: The ecology of dust. *Frontiers in Ecology and the Environment*, **8 (8)**, 423–430, https://doi.org/10.1890/090050.

Frie, A. L., J. H. Dingle, S. C. Ying, and R. Bahreini, 2017: The effect of a receding saline lake (the salton sea) on airborne particulate matter composition. *Environmental Science & Technology*, **51 (15)**, 8283–8292, https://doi.org/10.1021/acs.est.7b01773.

Frie, A. L., and Coauthors, 2019: Dust sources in the salton sea basin: a clear case of an anthropogenically impacted dust budget. *Environmental Science & Technology*, **53 (16)**, 9378–9388, https://doi.org/10.1021/acs.est.9b02137.

Giles, D. M., and Coauthors, 2019: Advancements in the aerosol robotic network (aeronet) version 3 database–automated near-real-time quality control algorithm with improved cloud screening for sun photometer aerosol optical depth (aod) measurements. *Atmospheric Measurement Techniques*, **12 (1)**, 169–209, https://doi.org/10.5194/amt-12-169-2019.

Giles, J., 2005: Climate science: The dustiest place on earth. *Nature*, **434 (7035)**, 816–820, https://doi.org/10.1038/434816a.

Ginoux, P., M. Chin, I. Tegen, J. M. Prospero, B. Holben, O. Dubovik, and S.-J. Lin, 2001: Sources and distributions of dust aerosols simulated with the gocart model. *Journal of Geophysical Research: Atmospheres*, **106 (D17)**, 20 255–20 273, https://doi.org/10.1029/2000JD000053.

Ginoux, P., J. M. Prospero, T. E. Gill, N. C. Hsu, and M. Zhao, 2012: Global-scale attribution of anthropogenic and natural dust sources and their emission rates based on modis deep blue aerosol products. *Reviews of Geophysics*, **50 (3)**, https://doi.org/10.1029/2012RG000388.

Gläser, G., P. Knippertz, and B. Heinold, 2012: Orographic effects and evaporative cooling along a subtropical cold front: The case of the spectacular saharan dust outbreak of march 2004. *Monthly Weather Review*, **140 (8)**, 2520–2533, https://doi.org/10.1175/MWR-D-11-00315.1.

Grell, G. A., 1993: Prognostic evaluation of assumptions used by cumulus parameterizations. *Monthly weather review*, **121 (3)**, 764–787, https://doi.org/10.1175/1520-0493(1993)121<0764:PEOAUB>2.0.CO;2.

Grell, G. A., and D. Dévényi, 2002: A generalized approach to parameterizing convection combining ensemble and data assimilation techniques. *Geophysical Research Letters*, **29 (14)**, 38–1, https://doi.org/10.1029/2002GL015311.

Grell, G. A., S. E. Peckham, R. Schmitz, S. A. McKeen, G. Frost, W. C. Skamarock, and B. Eder, 2005: Fully coupled "online" chemistry within the wrf model. *Atmospheric Environment*, **39 (37)**, 6957–6975, https://doi.org/10.1016/j.atmosenv.2005.04.027.

Grubišić, V., and B. J. Billings, 2007: The intense lee-wave rotor event of sierra rotors iop 8. *Journal of the atmospheric sciences*, **64 (12)**, 4178–4201, https://doi.org/10.1175/2006JAS2008.1.

Grubišić, V., and Coauthors, 2008: The terrain-induced rotor experiment: A field campaign overview including observational highlights. *Bulletin of the American Meteorological Society*, **89 (10)**, 1513–1534, https://doi.org/10.1175/2008BAMS2487.1.

Holben, B. N., and Coauthors, 1998: Aeronet–a federated instrument network and data archive for aerosol characterizatio. *Remote Sensing of Environment*, **66 (1)**, 1–16, https://doi.org/10.1016/S0034-4257(98)00031-5.

Horel, J., and Coauthors, 2002: Mesowest: Cooperative mesonets in the western united states. *Bulletin of the American Meteorological Society*, **83 (2)**, 211–225, https://doi.org/10.1175/1520-0477(2002)083<0211:MCMITW>2.3.CO;2.

Huneeus, N., and Coauthors, 2011: Global dust model intercomparison in aerocom phase i. *Atmospheric Chemistry and Physics*, **11 (15)**, 7781–7816, https://doi.org/10.5194/acp-11-7781-2011.

Iacono, M. J., J. S. Delamere, E. J. Mlawer, M. W. Shephard, S. A. Clough, and W. D. Collins, 2008: Radiative forcing by long-lived greenhouse gases: Calculations with the aer radiative transfer models. *Journal of Geophysical Research*, **113 (D13)**, https://doi.org/10.1029/2008JD009944.

IID, I. I. D., 2016: Salton sea air quality mitigation program. Tech. rep., Tech. Rep., Salton Sea Air Quality Team, 281 pp.

Janić, Z. I., 2001: *Nonsingular implementation of the Mellor-Yamada level 2.5 scheme in the NCEP Meso model*. US Department of Commerce, National Oceanic and Atmospheric Administration . . . .

Janjić, Z. I., 1994: The step-mountain eta coordinate model: Further developments of the convection, viscous sublayer, and turbulence closure schemes. *Monthly weather review*, **122 (5)**, 927–945, https://doi.org/10.1175/1520-0493(1994)122<0927:TSMECM>2.0.CO;2.

Jiang, H., J. T. Farrar, R. C. Beardsley, R. Chen, and C. Chen, 2009: Zonal surface wind jets across the red sea due to mountain gap forcing along both sides of the red sea. *Geophysical Research Letters*, **36 (19)**, https://doi.org/10.1029/2009GL040008.

Jiang, Q., J. D. Doyle, and R. B. Smith, 2006: Interaction between trapped waves and boundary layers. *Journal of the atmospheric sciences*, **63 (2)**, 617–633, https://doi.org/10.1175/JAS3640.1.

Jiang, Q., M. Liu, and J. D. Doyle, 2011: Influence of mesoscale dynamics and turbulence on fine dust transport in owens valley. *Journal of Applied Meteorology and Climatology*, **50 (1)**, 20–38, https://doi.org/10.1175/2010JAMC2522.1.

Jin, Y., and Coauthors, 2015: Ceilometer calibration for retrieval of aerosol optical properties. *Journal of Quantitative Spectroscopy and Radiative Transfer*, **153**, 49–56, https://doi.org/10.1016/j.jqsrt.2014.10.009.

Jones, B. A., and J. Fleck, 2020: Shrinking lakes, air pollution, and human health: Evidence from california's salton sea. *Science of the Total Environment*, **712**, 136 490, https://doi.org/10.1016/j.scitotenv.2019.136490.

Karyampudi, V. M., S. E. Koch, C. Chen, J. W. Rottman, and M. L. Kaplan, 1995: The influence of the rocky mountains on the 13–14 april 1986 severe weather outbreak. part ii: Evolution of a prefrontal bore and its role in triggering a squall line. *Monthly Weather Review*, **123 (5)**, 1423–1446, https://doi.org/10.1175/1520-0493(1995)123<1423:TIOTRM>2.0.CO;2.

Kim, K.-M., and Coauthors, 2021: Modeling asian dust storms using wrf-chem during the dragon-asia field campaign in april 2012. *Journal of Geophysical Research: Atmospheres*, **126 (18)**, e2021JD034 793, https://doi.org/https://doi.org/10.1029/2021JD034793.

Knippertz, P., 2014: Meteorological aspects of dust storms. *Mineral Dust*, P. Knippertz, and J. Stuut, Eds., Springer, 121–147, https://doi.org/10.1007/978-94-017-8978-3_6.

Knippertz, P., C. Deutscher, K. Kandler, T. Müller, O. Schulz, and L. Schütz, 2007: Dust mobilization due to density currents in the atlas region: Observations from the saharan mineral dust experiment 2006 field campaign. *Journal of Geophysical Research*, **112 (D21)**, https://doi.org/10.1029/2007JD008774.

Koch, S. E., P. B. Dorian, R. Ferrare, S. Melfi, W. C. Skillman, and D. Whiteman, 1991: Structure of an internal bore and dissipating gravity current as revealed by raman lidar. *Monthly Weather Review*, **119 (4)**, 857–887, https://doi.org/10.1175/1520-0493(1991)119<0857:SOAIBA>2.0.CO;2.

Kok, J., and Coauthors, 2014: An improved dust emission model–part 1: Model description and comparison against measurements. *Atmospheric Chemistry and Physics*, **14 (23)**, 13 023–13 041, https://doi.org/https://doi.org/10.5194/acp-14-13023-2014.

Kok, J. F., D. S. Ward, N. M. Mahowald, and A. T. Evan, 2018: Global and regional importance of the direct dust-climate feedback. *Nature Communications*, **9 (1)**, 1–11, https://doi.org/10.1038/s41467-017-02620-y.

LeGrand, S. L., C. Polashenski, T. W. Letcher, G. A. Creighton, S. E. Peckham, and J. D. Cetola, 2019: The afwa dust emission scheme for the gocart aerosol model in wrf-chem v3. 8.1. *Geoscientific Model Development*, **12 (1)**, 131–166, https://doi.org/10.5194/gmd-12-131-2019.

Marcos, C. R., J. L. Gómez-Amo, C. Peris, R. Pedrós, M. P. Utrillas, and J. A. Martínez-Lozano, 2018: Analysis of four years of ceilometer-derived aerosol backscatter profiles in a coastal site of the western mediterranean. *Atmospheric Research*, **213**, 331–345, https://doi.org/10.1016/j.atmosres.2018.06.016.

Marsham, J. H., P. Knippertz, N. S. Dixon, D. J. Parker, and G. M. Lister, 2011: The importance of the representation of deep convection for modeled dust-generating winds over west africa during summer. *Geophysical Research Letters*, **38 (16)**, https://doi.org/10.1029/2011GL048368.

Marticorena, B., and G. Bergametti, 1995: Modeling the atmospheric dust cycle: 1. design of a soil-derived dust emission scheme. *Journal of geophysical research: atmospheres*, **100 (D8)**, 16 415–16 430, https://doi.org/https://doi.org/10.1029/95JD00690.

Mayr, G. J., and L. Armi, 2010: The influence of downstream diurnal heating on the descent of flow across the sierras. *Journal of Applied Meteorology and Climatology*, **49 (9)**, 1906–1912, https://doi.org/10.1175/2010JAMC2516.1.

Mesinger, F., and Coauthors, 2006: North american regional reanalysis. *Bulletin of the American Meteorological Society*, **87 (3)**, 343–360, https://doi.org/10.1175/BAMS-87-3-343.

Miller, P., M. Williams, and T. Mote, 2021: Modeled atmospheric optical and thermodynamic responses to an exceptional trans-atlantic dust outbreak. *Journal of Geophysical Research: Atmospheres*, **126 (5)**, e2020JD032 909, https://doi.org/https://doi.org/10.1029/2020JD032909.

Monin, A. S., and A. M. Obukhov, 1954: Basic laws of turbulent mixing in the surface layer of the atmosphere. *Contrib. Geophys. Inst. Acad. Sci. USSR*, **151 (163)**, e187.

Münkel, C., N. Eresmaa, J. Räsänen, and A. Karppinen, 2007: Retrieval of mixing height and dust concentration with lidar ceilometer. *Boundary-Layer Meteorology*, **124 (1)**, 117–128, https://doi.org/10.1007/s10546-006-9103-3.

Nappo, C. J., 2013: *An introduction to atmospheric gravity waves*. Academic press.

NCEI, ????: U.s. climate normals. URL https://www.ncei.noaa.gov/products/land-based-station/us-climate-normals.

NCEP, 2013: Ncep office note 442: The gfs atmospheric model. Washington DC: sn.

Parajuli, S. P., and C. S. Zender, 2017: Connecting geomorphology to dust emission through high-resolution mapping of global land cover and sediment supply. *Aeolian Research*, **27**, 47–65, https://doi.org/https://doi.org/10.1016/j.aeolia.2017.06.002.

Parajuli, S. P., and C. S. Zender, 2018: Projected changes in dust emissions and regional air quality due to the shrinking salton sea. *Aeolian Research*, **33**, 82–92, https://doi.org/10.1016/j.aeolia.2018.05.004.

Peckham, S. E., and Coauthors, 1991: Wrf-chem version 3.9.1.1 user's guide. Tech. rep., National Center for Atmospheric Research. URL https://ruc.noaa.gov/wrf/wrf-chem/Users_guide.pdf.

Pokharel, A. K., M. L. Kaplan, and S. Fiedler, 2017: Subtropical dust storms and downslope wind events. *Journal of Geophysical Research: Atmospheres*, **122 (19)**, 10–191, https://doi.org/10.1002/2017JD026942.

Poudel, U., S. Ahmad, and H. Stephen, 2021: Studying the intra-annual variability in surface area and volume of salton sea, california, using remote sensing-based water indices and gis. *World Environmental and Water Resources Congress 2021*, 769–783, https://doi.org/10.1061/9780784483466.070.

Prospero, J. M., P. Ginoux, O. Torres, S. E. Nicholson, and T. E. Gill, 2002: Environmental characterization of global sources of atmospheric soil dust identified with the nimbus 7 total ozone mapping spectrometer (toms) absorbing aerosol product. *Reviews of geophysics*, **40 (1)**, 2–1–2–31, https://doi.org/10.1029/2000RG000095.

Pu, B., and P. Ginoux, 2018: How reliable are cmip5 models in simulating dust optical depth? *Atmospheric Chemistry and Physics*, **18 (16)**, 12 491–12 510, https://doi.org/10.5194/acp-18-12491-2018.

Ralph, F. M., P. J. Neiman, T. L. Keller, D. Levinson, and L. Fedor, 1997: Observations, simulations, and analysis of nonstationary trapped lee waves. *Journal of the atmospheric sciences*, **54 (10)**, 1308–1333, https://doi.org/10.1175/1520-0469(1997)054<1308:OSAAON>2.0.CO;2.

Ryerson, T., and Coauthors, 2013: The 2010 california research at the nexus of air quality and climate change (calnex) field study. *Journal of Geophysical Research: Atmospheres*, **118 (11)**, 5830–5866, https://doi.org/10.1002/jgrd.50331.

Scorer, R. S., 1949: Theory of waves in the lee of mountains. *Quarterly Journal of the Royal Meteorological Society*, **75 (323)**, 41–56, https://doi.org/10.1002/qj.49707532308.

Shao, Y., and Coauthors, 2011: Dust cycle: An emerging core theme in earth system science. *Aeolian Research*, **2 (4)**, 181–204, https://doi.org/10.1016/j.aeolia.2011.02.001.

Skamarock, W. C., and Coauthors, 2019: A description of the advanced research wrf model version 4. *National Center for Atmospheric Research: Boulder, CO, USA*, 145.

Smith, R. B., 2019: 100 years of progress on mountain meteorology research. *Meteorological Monographs*, **59**, 20–1, https://doi.org/10.1175/AMSMONOGRAPHS-D-18-0022.1.

Stephen, M. F., and D. S. Gorsline, 1975: Sedimentary aspects of the new river delta, salton sea, imperial county, california.

Strauss, L., S. Serafin, and V. Grubišić, 2016: Atmospheric rotors and severe turbulence in a long deep valley. *Journal of the Atmospheric Sciences*, **73 (4)**, 1481–1506, https://doi.org/10.1175/JAS-D-15-0192.1.

Sweeney, M. R., E. V. McDonald, and V. Etyemezian, 2011: Quantifying dust emissions from desert landforms, eastern mojave desert, usa. *Geomorphology*, **135 (1-2)**, 21–34, https://doi.org/10.1016/j.geomorph.2011.07.022.

Todd, M. C., R. Washington, S. Raghavan, G. Lizcano, and P. Knippertz, 2008: Regional model simulations of the bodélé low-level jet of northern chad during the bodélé dust experiment (bodex 2005). *Journal of Climate*, **21 (5)**, 995–1012, https://doi.org/10.1175/2007JCLI1766.1.

Wiegner, M., and Coauthors, 2014: What is the benefit of ceilometers for aerosol remote sensing? an answer from earlinet. *Atmospheric Measurement Techniques*, **7 (7)**, 1979–1997, https://doi.org/10.5194/amt-7-1979-2014.

Yang, S., J. Preißler, M. Wiegner, S. von Löwis, G. N. Petersen, M. M. Parks, and D. C. Finger, 2020: Monitoring dust events using doppler lidar and ceilometer in iceland. *Atmosphere*, **11 (12)**, 1294, https://doi.org/10.3390/atmos11121294.

Yuan, T., S. Chen, J. Huang, X. Zhang, Y. Luo, X. Ma, and G. Zhang, 2019: Sensitivity of simulating a dust storm over central asia to different dust schemes using the wrf-chem model. *Atmospheric Environment*, **207**, 16–29, https://doi.org/https://doi.org/10.1016/j.atmosenv.2019.03.014.

Zhao, A., C. L. Ryder, and L. J. Wilcox, 2022: How well do the cmip6 models simulate dust aerosols? *Atmospheric Chemistry and Physics*, **22 (3)**, 2095–2119, https://doi.org/10.5194/acp-22-2095-2022.

Zucca, C., N. Middleton, U. Kang, and H. Liniger, 2021: Shrinking water bodies as hotspots of sand and dust storms: The role of land degradation and sustainable soil and water management. *Catena*, **207**, 105 669, https://doi.org/10.1016/j.catena.2021.105669.